Title

Local synthesis of Reticulon-1C lessens the outgrowth of injured axons and Spastin activity

Authors

Alejandro Luarte[1,2,3]*, Javiera Gallardo[8], Daniela Corvalán[1,2], Ankush Chakraborty [1,2], Cláudio Gouveia-Roque[5], Francisca Bertin[11], Carlos Contreras[1,2], Juan Pablo Ramírez [1,2], Andrè Weber [20], Waldo Acevedo[8], Werner Zuschratter[19], Rodrigo Herrera-Molina[9,10], Úrsula Wyneken [1,2,3] Andrea Paula-Lima [16,17], Tatiana Adasme-Rocha[18], Jorge Toledo[21], Rodrigo Vergara[22] , Antonia Figueroa[1,2], Carolina González[15], Christian González-Billault[4, 12, 13, 14], Ulrich Hengst [5,6], and Andrés Couve [4]

Affiliations

1 Faculty of Medicine, Universidad de los Andes, Santiago 7620001, Chile
2 Program in Neuroscience, Center for Biomedical Research, and Innovation (CiiB), Universidad de los Andes, Santiago 7620001, Chile
3 IMPACT, Center of Interventional Medicine for Precision and Advanced Cellular Therapy, Santiago 7620001, Chile
4 Department of Neuroscience, Faculty of Medicine, Universidad de Chile, Santiago, Chile.
5 The Taub Institute for Research on Alzheimer's Disease and the Aging Brain, Columbia University Vagelos College of Physicians and Surgeons, New York, NY 10032, USA
6 Department of Pathology and Cell Biology, Columbia University Vagelos College of Physicians and Surgeons, New York, NY 10032, USA
7 Instituto de Química, Facultad de Ciencias, Pontificia Universidad Católica de Valparaíso, Valparaíso 2373223, Chile
8 Centro de Medicina Regenerativa, Facultad de Medicina, Clínica Alemana-Universidad del Desarrollo, Santiago, Chile
9 Centro Integrativo de Biología y Química Aplicada, Universidad Bernardo O'Higgins, 8307993 Santiago, Chile
10 Department of Pharmacology & Physiology, George Washington University, Ross Hall, Washington, DC, USA
11 Facultad de Medicina Veterinaria y Agronomía, Universidad de Las Américas, sede Providencia, Manuel Montt 948, 7500975, Santiago, Chile
12 Department of Biology, Faculty of Sciences, Universidad de Chile, Santiago, Chile
13 Public Nutrition Unit, Institute for Nutrition and Food Technologies, Universidad de Chile, Santiago, Chile
14 The Buck Institute for Research on Aging, Novato, USA
15 Latin American Brain Health Institute (BrainLat), Universidad Adolfo Ibañez, Santiago, Chile
16 Biomedical Neuroscience Institute and Department of Neurosciences, Faculty of Medicine, Universidad de Chile, Santiago 8380000, Chile
17 Institute for Research in Dental Sciences (ICOD), Faculty of Dentistry, Universidad de Chile, Santiago 8380544, Chile
18 Oficina de apoyo a la investigación clínica, hospital clínico universidad de Chile, Santiago 8380494, Chile
19 Leibniz Institute for Neurobiology, 39118 Magdeburg, Germany
20 Photonscore GmbH, Brenneckestr. 20, 39118 Magdeburg, Germany
21 Health Sciences Department, Universidad de Aysén, Coyhaique, Chile.
22 Departamento de Kinesiología, Facultad de Artes y Educación Física, Universidad Metropolitana de Ciencias de la Educación

*Corresponding author at: Faculty of Medicine, Universidad de los Andes, Santiago 7620001, Chile. aluarte@uandes.cl

Abstract

The regenerative potential of developing cortical axons following injury depends on intrinsic mechanisms, such as axon-autonomous protein synthesis, that are still not fully understood. An emerging factor in this regenerative process is the bi-directional interplay between microtubule dynamics and the delicate morphology of the axonal endoplasmic reticulum (ER). Therefore, we hypothesize that locally synthesized ER structural proteins regulate microtubule dynamics and the regenerative response of cortical axons. This hypothesis is supported by RNA data-mining, which identified *Reticulon-1* as the sole mRNA coding for an ER-shaping protein across eight axonal transcriptomes and found it to be downregulated following injury. Using compartmentalized microfluidic chambers, we demonstrate that local knockdown of *Reticulon-1* mRNA increases the outgrowth while reducing the distal tubulin levels of injured axons. Furthermore, we show by live-cell imaging that axonal *Reticulon-1* knockdown restores the loss of microtubule growth speed and length caused by injury. Interestingly, axonal inhibition of the microtubule-severing protein Spastin fully prevents the effects of axonal *Reticulon-1* knockdown on outgrowth as well as distal tubulin levels, while not affecting most of the analyzed microtubule dynamic parameters. Further, we demonstrate that the Reticulon-1C isoform is locally synthesized within axons and provide evidence supporting that it attenuates Spastin-mediated microtubule severing. These findings uncover a mechanism by which the local synthesis of an ER-shaping protein provides fine control over cortical axon regeneration.

Introduction

Developing cortical axons can regenerate after injury but lose this capacity at later stages (Cooke et al., 2022). The regenerative potential of developing axons depends on extrinsic and intrinsic (cell autonomous) factors that regulate their outgrowth (He & Jin, 2016). The structure of the axonal endoplasmic reticulum (ER) is a determinant intrinsic factor for regulating outgrowth during development and after injury (Aridor & Fish, 2009; Deitch & Banker, 1993a; Krijnse-Locker et al., 1995; Nozumi et al., 2009; Petrova et al., 2020; Rao et al., 2016a). Indeed, ER proteins are locally synthesized in axons and may contribute to regeneration (Pacheco et al., 2020; Willis et al., 2005). However, the role of axonal protein synthesis in shaping ER function after injury remains largely unexplored.

Unlike the ribosome-rich somato-dendritic ER, the structure of the axonal ER predominantly comprises continuous tubules of smooth ER, maintained by specific ER-shaping proteins (Voeltz et al., 2006; Wu et al., 2017). As such, the mostly tubular axonal ER controls calcium handling, lipid provision, and potentially transmembrane protein supply, which contribute to axon elongation (Cornejo et al., 2017; de Juan-Sanz et al., 2017; González et al., 2016; Luarte et al., 2018a). More recently, a bi-directional relationship of the axonal ER with microtubule dynamics has emerged as critical for regulating outgrowth. For instance, the physical coupling of the axonal ER to growing microtubules through STIM1 determines its positioning into filopodia in growth cones to control the guidance of developing axons (Pavez et al., 2019). In turn, the axonal ER controls microtubule dynamics, which is required for axonal specification and proper outgrowth in response to injury (Farías et al., 2019a; Rao et al., 2016a).

Different lines of evidence support that the protein components of the axonal ER may interact with proteins that regulate microtubule dynamics[20,21]. For instance, the interaction of ER structural proteins with microtubule severing enzymes may contribute to sculpt the axonal cytoskeleton required for outgrowth (Rao et al., 2016b; Stone et al., 2012a). As such, the microtubule-severing protein Spastin is known to interact with different ER-shaping proteins (Evans et al., 2006; Mannan et al., 2006a), but the contribution of axonal protein synthesis to this process has not been addressed. Here, we hypothesized that the local synthesis of ER structural proteins controls microtubule dynamics and the elongation of injured axons. Using a variety of techniques, we report that local synthesis of the ER-shaping protein Reticulon-1 (Rtn-1) controls microtubule dynamics and the outgrowth of injured cortical axons depending on Spastin-mediated microtubule severing.

Results

Rtn-1 mRNA is consistently identified in axonal transcriptomes

We hypothesized that the local synthesis of an ER structural protein controls microtubule dynamics and the elongation of injured axons. As a first approach to test our hypothesis, we looked for mRNAs coding for ER structural proteins in reported axonal transcriptomes from different species, developmental stages, and days *in vitro* (DIV) as indicated in Table I. To enhance the robustness of our analysis, we focused on transcripts that were consistently identified across conditions through Benjamini–Hochberg (Ben) analysis. We identified 104 common mRNAs across all studies (Figure 1A) and classified them under the 'Cellular Component' category using Gene Ontology (GO) analysis. We found that *Rtn-1* mRNA was the only transcript coding for an ER structural protein that is shared across all the samples (Figure 1B). Note that several of the identified transcripts in the category 'endoplasmic reticulum' code for cytoplasmic ribosomal components, which indeed can be attached to the axonal ER (Koppers et al., 2024) and be locally synthesized in axons (Shigeoka et al., 2019). On a similar approach, but combining data from dendrites and axons, it was found that *Reticulon-3* mRNA is present in 16 out of 20 studies, further suggesting a wider presence of ER-shaping protein mRNAs in axons (von Kügelgen & Chekulaeva, 2020). Interestingly, one of the studies presented in (Figure 1B) showed that *Rtn-1* mRNA levels in cortical axons are decreased by 5.26 ± 0.06-fold after axotomy (Taylor et al., 2009a). Thus, *Rtn-1* mRNA is consistently identified in intact axons, and it is down-regulated upon injury.

Next, we studied the distribution of Rtn-1 protein in axons from cultured rat cortical neurons at early developmental stages. To this end, we assessed the fluorescence intensity of Rtn-1 along the terminal 50 µm of distal axons at 1, 3, and 7 days *in vitro* (DIV). Axonal identity was confirmed by β3-tubulin and the absence of the dendritic marker microtubule-associated protein 2 (MAP2). Rtn-1 fluorescence was concentrated in the most distal axonal region corresponding to the growth cone (GC), which is significantly more pronounced at 7 DIV compared to 1 DIV (Supplementary figure 1 A-C). Rtn-1 enrichment within GCs diverged from the staining pattern of KDEL, a luminal ER marker, which did not exhibit such progressive accumulation (Supplementary figure 1 A-C). The distribution of Rtn-1 agreed with prior studies that localized this protein at the base of the GC's hand-like structure, as outlined by the actin cytoskeleton stained with phalloidin (Nozumi et al., 2009) (Supplementary figure 1D). This distribution supports a model where Rtn-1 contributes to the dense network of ER tubules characteristically found in the GCs, an observation well-documented in earlier studies(Deitch & Banker, 1993a)

148 **Axonal synthesis of Rtn-1 lessens outgrowth after injury**

149

150 To elucidate the role of Rtn-1 synthesis in the outgrowth of injured axons, we first
151 validated knockdown (KD) of this protein by Western blot (WB) in cultured cortical neurons.
152 Neuronal Rtn-1 isoforms include isoform A (Rtn-1A), comprising 776 amino acids, and isoform
153 C (Rtn-1C) with 208 amino acids. Both isoforms share a highly conserved C-terminal region
154 known as the Reticulon homology domain (RHD), differing only in their 20 N-terminal amino
155 acids (Chiurchiù et al., 2014; Roebroek et al., 1993a; Van De Velde et al., 1994a). Thus, we
156 transfected 7 DIV dissociated cortical neurons with siRNAs designed to target the conserved RHD
157 domain (i.e., siRNAs that target all Rtn-1 isoforms) or a control sequence (scrambled, Scr). Forty-
158 eight hours later, samples were analyzed using a pan-Rtn-1 antibody raised against the conserved
159 RHD region. Two distinct Rtn-1 bands were observed: a higher molecular weight band near 180
160 kDa, likely representing Rtn-1A (Van De Velde et al., 1994b), and a lower band near 24 kDa,
161 corresponding to the apparent molecular weight of Rtn-1C (Roebroek et al., 1993b; Van De Velde
162 et al., 1994b) (Figure 2A). As expected, siRNAs reduced Rtn-1 for both isoforms when compared
163 to Scr, with the siRNA 2 demonstrating a slight trend toward greater efficacy than siRNA 1 when
164 quantifying the band corresponding to Rtn-1C isoform (lower molecular weight) (Figure 2A).
165 Immunofluorescence staining further revealed a marked decrease in Rtn-1 intensity in the cell
166 body and distal axons of neurons co-transfected with an RFP-expressing plasmid and siRNA 2
167 under the same conditions (Figure 2B). Therefore, unless otherwise indicated, for all subsequent
168 experiments siRNA 2 was used to downregulate Rtn-1.

169

170 We then performed KD of Rtn-1 selectively within the axonal compartment (axonal Rtn-
171 1 KD) in 7 DIV microfluidic chamber cultures. This compartmentalized approach has been
172 validated in multiple studies to locally control neuronal protein synthesis (Baleriola et al., 2014;
173 Batista et al., 2017; Zhang et al., 2013a) .Twenty-four hours later, we found that axonal Rtn-1 KD
174 did not alter somatic Rtn-1 levels yet elicited a significant ~ 25% decrease in somatic β3-tubulin,
175 which were quantified as the intensity fold change for both proteins compared to Scr (Figure 2C).
176 Compatible with Rtn-1 local synthesis, axonal Rtn-1 KD led to a significant ~ 46% decrease in
177 its fluorescence intensity within the distal 50 μm of axons, which was depicted by the corrected
178 fluorescence intensity profile and quantified as the intensity fold change compared to Scr (Figure
179 2D and E). A slight but significant ~ 16% decrease in β3-tubulin fluorescence intensity fold
180 change was also observed after axonal Rtn-1 KD compared to Scr (Figure 2D and E). These
181 results support that local synthesis of Rtn-1 can be locally downregulated in the axonal
182 compartment and suggest an interplay with the organization of the microtubule cytoskeleton.

183

184 To investigate the role of local Rtn-1 synthesis in axonal outgrowth, we subjected 8 DIV
185 cortical axons to axotomy by vacuum aspiration in microfluidic chambers. To this end, we
186 simultaneously performed Rtn-1 KD in either axonal or somato-dendritic compartments and
187 measured outgrowth twenty-four hours later (Figure 3A). To measure outgrowth, we performed
188 Sholl analysis (McCurdy et al., 2019; Sholl, 1953) and quantified the summatory of the
189 intersections of binarized axons with concentric semi-circles of increasing radius centered at the
190 microgroove exit of the microfluidic chambers (Figure 3B). Interestingly, we observed a
191 significant increase in outgrowth (higher number of intersections summatory) within the 500-
192 1000 µm and 1000-1500 µm ranges with axonal Rtn-1 KD compared to Scr (Figure 3B).
193 Furthermore, this response was specific for the axonal compartment, as somatic Rtn-1 KD showed
194 a non-significant effect with a slight opposite trend (Figure 3C).
195
196 To discard off-target effects of siRNA used for axonal Rtn-1 KD, we validated a third
197 and completely different oligonucleotide sequence (siRNA 3) directed against Rtn-1 and tested
198 its capacity to reproduce the observed phenotype with local KD in injured axons. We found by
199 WB that this sequence significantly decreased Rtn-1C levels, while Scr and non-transfected
200 neurons did not. Also, no significant changes of β3-tubulin levels were observed (Supplementary
201 figure 2 A-B). Of note, blots were normalized to the total amount protein per lane, suggesting that
202 siRNA 3 does not have unspecific effects on β3-tubulin levels. To test the ability of siRNA 3 to
203 promote outgrowth, we selectively treated axotomized axons in microfluidic chambers and
204 measured outgrowth twenty-four hours after injury. Axonal KD performed with siRNA 3
205 resembled the overall outgrowth tendency observed with siRNA 2 (Figures 3 A-B). As such, it
206 was observed a significant increase in the summatory of axonal intersections within the 0-500 µm
207 and 500-1000 µm ranges after axonal Rtn-1 KD compared to Scr (Supplementary figure 2 C-
208 D). Together, these results suggest that the increased outgrowth of injured axons observed with
209 axonal KD is not likely due to siRNA off-target effects.
210
211 To further characterize the role of axonally synthesized Rtn-1 in injured axons, we
212 assessed the morphology of GCs in the same experimental setting described above. To this end,
213 we used β3-tubulin immune staining and phalloidin incubation to reveal the actin cytoskeleton.
214 Axonal Rtn-1 KD did not modify the perimeter (outline) and the area of GCs. However, axonal
215 Rtn-1 KD produced GCs characterized by a more elongated and compact actin cytoskeleton,
216 reflected on a significant increase in the elongation ratio (calculated as the length of the major
217 axis divided by the length of the minor axis of the best-fitting ellipse to the actin boundary) and
218 longest shortest path (LSP, which reflects the maximum length of the skeletonized actin outline),
219 alongside with a reduced number of filopodia (Figure 3D). Collectively, these morphometric
220 parameters revealed that axonal Rtn-1 KD yielded GCs resembling a spade-like morphology that

221 has been previously related to increased outgrowth (Kaethner & Stuermer, 1992). Compatible
222 with this idea, somatic Rtn-1 KD did not promote outgrowth nor modified any of these
223 morphological parameters, except for an increase in the GC LSP (Figure 3D). Together, these
224 results suggests that axonal synthesis of Rtn-1 is normally acting to repress the outgrowth of
225 injured axons.
226
227 **Axonal Rtn-1 KD decreases β3-tubulin levels in injured axons**
228
229 The previously-described changes on β3-tubulin elicited by axonal Rtn-1 KD before
230 injury (Figure 2D), lead us to examine β3-tubulin and Rtn-1 fluorescence intensity under this
231 condition in axotomized axons. Different from what we observed in intact axons (Figure 2D and
232 E), twenty-four hours of axonal Rtn-1 KD did not alter Rtn-1 fluorescence significantly, but it
233 induced a ~ 20 % reduction in β3-tubulin intensity compared to Scr (Figure 4A). In contrast,
234 somatic Rtn-1 KD did decrease Rtn-1 fluorescence in axons by ~ 33% (Figure 4B), supporting
235 the notion that most of axonal Rtn-1 protein originates in the soma. Of note, somatic Rtn-1 KD
236 also decreased β3-tubulin intensity by ~ 19% in axons (Figure 4B).
237
238 Consistent with a potential compensatory response of the cell body specifically on injured
239 neurons, axonal Rtn-1 KD leads to increased somatic Rtn-1 fluorescence compared to Scr (Figure
240 4C). This somatic increase may partially explain the lack of changes on axonal Rtn-1 levels after
241 twenty-four hours of local KD (Figure 4A), which is potentially countered by somatic Rtn-1
242 synthesis and transport towards the axon. Intriguingly, resembling the somatic increase of Rtn-1,
243 β3-tubulin levels were also elevated in the cell bodies following axonal Rtn-1 KD compared to
244 Scr (Figure 4C). In contrast, somatic Rtn-1 KD resulted in a significant reduction in the somatic
245 fluorescence intensity for both proteins compared to Scr (Figure 4D). Together, these results
246 indicate that after axonal injury, the levels of Rtn-1 in the somatic and axonal compartments tend
247 to change in a manner that parallels β3-tubulin, which suggests a mechanistic relationship
248 between these two proteins.
249
250 **Rtn-1 axonal synthesis shields Spastin microtubule severing impacting on outgrowth**
251
252 The significant alterations in β3-Tubulin levels after Rtn-1 KD in the context of injury,
253 led us to explore the role of Rtn-1 interactors that can modify the microtubule cytoskeleton.
254 Notably, a previous study had shown by yeast two hybrid assay that a protein sequence from Rtn-
255 1C directly interacts with the microtubule-severing protein Spastin (Mannan et al., 2006b).
256 Therefore, we explored the localization of Spastin and Rtn-1C in distal axons before and after
257 injury.

258

259 To this end, we stained 8 DIV non-injured and injured axons (submitted to axotomy at 7
260 DIV) against Spastin (all isoforms) and Rtn-1C to perform Stimulated Emission Depletion
261 (STED) super-resolution microscopy. In both conditions, Rtn-1C and Spastin showed a clear
262 enrichment of the staining in the GC (Figure 5A, left panel). The distribution of Rtn-1C along the
263 axonal shaft is fine and continuous, consistent with its localization in ER tubules, which appear
264 decorated with clusters of Spastin. In contrast to the more central positioning of Rtn-1C in the
265 axonal shaft, Spastin displays a broader distribution in both conditions (Figure 5A, left panel).
266 This difference is also seen in the GCs, where Rtn-1C is more concentrated at the center of these
267 domains (Figure 5A, left panel). In injured axons, distal Rtn-1C staining appears less compact,
268 adopting a more tubulated pattern (Figure 5A, left panel). Moreover, following injury, Rtn-1C
269 staining seems slightly retracted from the GC compared to the non-injured condition, as also
270 suggested by its relative intensity profile (Figure 5A, right panel). Spastin distribution along the
271 distal axon remains largely similar between conditions (Figure 5A, right panel). However, in
272 injured axons, Spastin appears less diffuse and more concentrated in clusters than in non-injured
273 axons (Figure 5A left and right panel). No significant changes were observed when analyzing the
274 total fluorescence intensity of both proteins (Supplementary figure 4). These findings indicate
275 that both proteins are enriched in the GC and closely apposed along the axonal shaft. Although
276 we did not directly test their molecular association, these results are consistent with Rtn-1C and
277 Spastin sharing a similar subcellular localization, potentially enabling their functional interaction
278 in distal axons.

279

280 To elucidate the potential connection of Rtn-1 axonal synthesis KD with Spastin's
281 microtubule-severing activity, we took advantage of a Spastazoline (SPTZ), a well-characterized
282 and specific inhibitor of the ATPase activity of Spastin (i.e., microtubule severing)(Cupido et al.,
283 2019). Under these conditions, we monitored the changes in the fluorescence intensity of β3-
284 tubulin, Rtn-1C, and Spastin forty-eight hours post-axonal injury. Note that these experiments
285 were performed in a two-fold longer period compared to those shown in Figure 4. This extended
286 time was taken to i) to reveal more clearly the changes in β3-tubulin content and ii) to allow the
287 proper expression of the EB3-Emerald plasmid which was used for the live-cell imaging
288 experiment that will be described later in Figure 5. We found that axonal Rtn-1 KD resulted in a
289 ~ 60% reduction in β3-tubulin levels within the distal 50µm of axons, compared to controls (Scr
290 and DMSO) (Figure 5B). However, co-incubation with 50 nM SPTZ (applied four hours after
291 axotomy) completely abolished the β3-tubulin reduction elicited by axonal Rtn-1 KD, while it did
292 not alter Rtn-1C and Spastin levels (Figure 5B). This rescue of β3-tubulin levels during axonal
293 Rtn-1 KD by a specific drug (SPTZ), makes unlikely that this reduction is produced by an off-
294 target effect of the siRNA. If this was the case, this potential off-target effect should be still

295 operating in the presence of SPTZ. Also discarding unspecific effects over the implicated proteins,
296 SPTZ administration alone did not significantly modified β3-tubulin levels, nor those of Rtn-1C
297 and Spastin (Figure 5B). Together, these observations suggest that axonal Rtn-1 KD correlates
298 with reduced inhibition of Spastin microtubule severing.
299
300 Next, we aimed at exploring whether the increased outgrowth elicited by axonal Rtn-1
301 KD after injury depended on Spastin's microtubule severing. To this end, we studied the effects
302 of axonal Rtn-1 KD on outgrowth forty-eight hours after axotomy by Sholl analysis. In contrast
303 with the effects observed after twenty-four hours of axotomy (Figure 3A), after forty-eight hours
304 of axonal Rtn-1 KD there was only a trend (non-statistically significant) to increase outgrowth in
305 the 1000-1500 µm range compared to controls (Figure 5 C and D). However, local co-incubation
306 of 50 nM SPTZ with axonal Rtn-1 KD abolished this trend, producing a statistically significant
307 outgrowth decrease compared to the axonal Rtn-1 KD / DMSO condition (Figure 5 C and D).
308 Local SPTZ application in axons treated with a Scr sequence displayed a trend to increase outgrow
309 compared to all the conditions, particularly in the 1000-1500 µm segment, but any of these
310 comparisons reached statistical significance (Figure 5C and D). Together, these results suggest
311 that locally synthesized Rtn-1 would normally act to suppress the outgrowth of injured axons by
312 restricting the microtubule severing activity of Spastin.
313
314 Considering the observed shifts in microtubule content and the previously reported role
315 of Spastin in controlling microtubule stability (Aiken & Holzbaur, 2024; Kuo et al., 2019a;
316 Teixeira Lopes, 2018), we aimed at quantifying microtubule dynamics by live-cell imaging before
317 and after injury. To this end, cortical neurons cultured in microfluidic chambers were transfected
318 at 7 DIV with a plasmid coding for the microtubule tip-binding protein EB3 fused to the
319 fluorescent construct Emerald GFP (EB3-GFP), which labels the growing plus-ends of
320 polymerizing microtubules(Stepanova et al., 2003). Axotomy was performed at 8 DIV, and
321 immediately, axons were locally transfected with a Rtn-1 siRNA or Scr sequence. Non-injured 8
322 DIV axons were transfected in parallel. Four hours after transfection, non-injured and injured
323 axons were either treated with DMSO (control) or 50 nM SPTZ. Then forty-eight hours since
324 injury (10 DIV), axons were directly imaged in microfluidic chambers to examine the dynamic
325 behavior of EB3-GFP puncta (comets).
326
327 We first analyzed the effect of axonal Rtn-1 KD on non-injured axons. Interestingly, we
328 found that axonal Rtn-1 KD elicited a statistically significant increase on microtubule growth
329 speed, while it did not significantly modified microtubule track length and lifetime compared to
330 controls (Scr + DMSO) (Figure 5E). To reveal the role of Spastin's microtubule severing in
331 modifying these parameters, we co-incubated axons with 50 nM SPTZ. As such, SPTZ treatment

332 did not prevent the increase on microtubule growth speed elicited by axonal Rtn-1 KD nor
333 modified comet's lifetime but induced a significant increase on track length when compared to
334 controls (Figure 5E).
335 Next, we analyzed the effect of axonal Rtn-1 KD on comet parameters after injury. In
336 contrast with the milder increase observed in non-injured axons, axonal Rtn-1 KD augmented by
337 nearly two-fold the growth speed and track length of microtubules, while it did not modify comet
338 lifetime compared controls (Figure 5E, left and right panels). Of note, compared to non-injured
339 axons, growth speed and track length are significantly decreased on axotomized axons (from 0.09
340 to 0.06 µm/s, and from 4.6 µm to 2,6 µm; $p<0.0001$, Mann Whitney test), compatible with axonal
341 damage promoting a more unorganized or less processivity of microtubule growth(Rolls et al.,
342 2020; Yap et al., 2017). SPTZ co-treatment did not prevent the increase on microtubule growth
343 speed and track length elicited by axonal Rtn-1 KD after injury compared to controls, nor
344 modified comet's lifetime (Figure 5E, right panels). However, SPTZ treatment along with axonal
345 Rtn-1 KD did induce a significant increase on comet lifetime when compared to axonal Rtn-1 KD
346 +DMSO as shown in right panels of figure 5E. Thus, axonal Rtn-1 synthesis control microtubule
347 dynamic parameters in non-injured and injured axons mostly independently of Spastin
348 microtubule severing.
349
350 Collectively, these results indicate that Rtn-1 would counteract Spastin's severing
351 function locally in axons, impacting on outgrowth. Previous evidence points to a specific role for
352 the Rtn-1C isoform in this mechanism (Mannan et al., 2006b). However, it is unknown which
353 locally synthesized Rtn-1 isoform may control Spastin's function in axons.
354
355 **The Reticulon-1 isoform C (Rtn-1C) is locally synthesized in cortical axons**
356
357 We first characterized the *Rtn-1* mRNA expression in axons. To this end, we employed a
358 culture technique for producing 'neuronballs'. This methodology facilitated the segregation of an
359 axon-enriched fraction through mechanical separation from the somato-dendritic structures
360 (Sasaki et al., 2010). The axonal compartment of desomatized neuronballs was identified by IF
361 against medium chain neurofilament (NF-M), while the somato-dendritic compartment was
362 stained with microtubule-associated protein 2 (MAP2) (Figure 6A). RNA was then extracted from
363 both the axonal and somato-dendritic fractions and submitted to reverse transcription PCR (RT-
364 PCR). The purity of the axonal fraction was evidenced by the absence of amplification for *Map2*,
365 *Histone h1(*general nuclei marker), and the astrocyte-specific glial fibrillary acidic protein (*Gfap*)
366 mRNAs. In contrast, we found positive amplification for *β-actin* transcript, which is known to be
367 present in axonal compartment (Figure 6A). These fractions were further analyzed with *Rtn-1*
368 specific primers targeted against C-terminal domain or the N-terminal domain (to reveal *Rtn-1A*).

369 In contrast to the somato-dendritic fraction, axons did not amplify for *Rtn-1A* mRNA, suggesting
370 that *Rtn-1C* transcript is the predominant isoform in this compartment (Figure 6A)
371 Next, we investigated the protein composition of the axonal and somato-dendritic
372 fractions by WB. Consistent with the sample purity observed for mRNAs, the axonal fraction was
373 positive for Tau and β3-tubulin, with no detection of the dendritic marker MAP 2 (Figure 6A).
374 For Rtn-1 identification, we employed a pan-Reticulon-1 antibody targeting the conserved C-
375 terminal Reticulon homology domain (RHD). Importantly, the axonal fraction showed exclusivity
376 for the lower molecular weight band, indicative of Rtn-1C presence, mirroring RT-PCR results
377 (Figure 6A). Immunofluorescence analysis of Rtn-1C in 8 DIV cortical axons, prepared in
378 microfluidic chambers, displayed a distribution pattern consistent with that of the pan-Reticulon-
379 1 (Rtn-1 antibody), as illustrated in Figure 2 (Figure 6B). In contrast, Rtn-1A presence was limited
380 to a small subset of axons, exhibiting a peak of localization near the growth cone base (Figure
381 6B). Thus, resembling the distribution of transcripts, Rtn-1C protein appears as the predominant
382 isoform in the axonal compartment.
383
384 In figure 2 we provided evidence compatible with the axonal synthesis of Rtn-1 in cortical
385 axons. In addition, we showed that the predominant mRNA and protein in cortical axons
386 correspond to the Rtn-1C isoform (Figure 6 A and B). However, whether Rtn-1C is indeed locally
387 synthesized in cortical axons has not been proved.
388 To demonstrate the local production of Rtn-1C in axons, we employed a proximity
389 ligation assay integrated with puromycilation (puro-PLA) (Dieck et al., 2015). During this assay,
390 we selectively administered a puromycin pulse (15 minutes) to the axonal or somato-dendritic
391 compartment of microfluidic chambers, allowing its covalent incorporation into nascent
392 polypeptides. This enabled the detection of newly synthesized Rtn-1C peptides through
393 fluorescent signals produced by the nanometric proximity (~40 nm) of puromycin and Rtn-1C
394 antibodies (Figure 6C). Positive amplification was observed in the somato-dendritic compartment
395 of microfluidic chambers with local puromycin treatment as dots or puncta (Figure 6D, left panel).
396 However, virtually no signal was detected in the cell bodies when puromycin was added to the
397 axonal compartment, showing the effective compartmentalization of this approach (Figure 6D,
398 left panel). Positive signal in the cell bodies was abrogated when the protein synthesis inhibitor
399 emetine was previously added, further supporting that these signals reflect protein synthesis
400 (Figure 6D, left panel). Supporting its local synthesis, fluorescent puncta were observed in axons,
401 which was significantly reduced by previous emetine treatment (Figure 6D, right panel).
402 Interestingly, when the puromycin pulse was applied exclusively to the somatic compartment,
403 positive signal was still detected in axons but in a significantly lower amount compared to direct
404 and puromycin/emetine treatments (Figure 6D, right panel). This suggests that at least a fraction
405 of puromycylated peptides synthesized in the cell bodies may rapidly (within 15 minutes) reach

406 the axons through as-yet uncharacterized mechanisms. Nevertheless, the significantly stronger
407 signal detected in the axonal compartment with direct puromycin treatment is fully consistent
408 with local Rtn-1C synthesis in axons.
409 To further validate puro-PLA detection, we tested the Rtn-1C antibody specificity by WB
410 and IF, and whether puro-PLA signals depended on local depletion of *Rtn-1* mRNA (axonal Rtn-
411 1 KD). Due to their low background for neuronal components, we used COS-7 cells expressing
412 the rat Rtn-1C protein fused to GFP (Rtn-1C-GFP) and analyzed them by WB, using the same
413 Rtn-1C antibody of the puro-PLA experiment. As expected, a single band of the predicted
414 molecular weight for the recombinant protein was observed in the lane of transfected cells, while
415 no band was apparent in non-transfected cells (Supplementary figure 3A). Also, revealing an
416 isoform-specific immunodetection, the ER pattern depicted by Rtn-1C-GFP fully overlapped with
417 the IF using the Rtn-1C antibody (Supplementary figure 3B). Similar results were observed for
418 Rtn-1A-GFP expressing COS-7 cells stained against Rtn-1A antibody (Supplementary figure 3B).
419 Of note, when we performed crossed antibody staining of Rtn-1 isoforms on transfected cells, no
420 positive staining was found (Data not shown). We also tested the specificity of this antibody by
421 transfecting these cells with the previously validated siRNA 2 sequence. As expected, siRNA 2
422 induced a significant decrease of Rtn-1C compared to Scr (Supplementary figure 3C). Finally, 9
423 DIV axons were locally treated in microfluidic chambers with siRNA2 for twenty-four hours,
424 which produced a significant decrease of positive puro-PLA signal compared to Scr
425 (Supplementary figure 3D). Together, these results confirm that the quantified puro-PLA signal
426 is indeed reflecting the local translation of *Rtn-1C* mRNA in axons.
427
428 **Rtn-1C but not Rtn-1A shields the microtubule severing activity of Spastin**
429
430 We established that Rtn-1C is locally synthesized in cortical axons, while Rtn-1A
431 synthesis should predominantly occur in the cell body. Therefore, we aimed at understanding the
432 functional implications of such compartmentalization. We chose COS-7 cells as a heterologous
433 system because of their increased co-transfection efficiency, flat and extended morphology, and
434 low background of neuronal proteins. These features provided an advantageous context to
435 visualize ER protein distribution and functional relationships.
436
437 Thus, we first over-expressed in COS-7 cells an RFP-tagged version of the most abundant
438 Spastin isoform during neuronal development, which corresponds to M87 isoform. Of note, in
439 contrast to M1 isoform, M87 isoform is fully soluble and devoid of the ER-shaping membrane
440 domain (Solowska et al., 2017). Next, the plasmid coding for isoform M87 was co-transfected
441 with Rtn-1C-GFP, Rtn-1A-GFP or GFP alone. Spastin-RFP displayed a punctate distribution
442 when co-expressed with GFP, indicative of its potential interaction with endosomal components,

443 as reported elsewhere (Allison et al., 2013) (Figure 7A, upper panels). Under this condition,
444 Spastin puncta strongly co-distributed with some clusters of soluble GFP. It has been described
445 that under certain circumstances soluble proteins such as GFP might be bulk up taken by late
446 endosomal structures (Sahu et al., 2011), which are also known to be positive for M87 Spastin
447 (Allison et al., 2019). To rule out that, in our case, this co-distribution is due to fluorescence
448 crosstalk, we independently acquired images for each fluorophore in co-transfected cells. We
449 observed that COS-7 cells co-transfected with Spastin-RFP and GFP displayed the same
450 previously described puncta for both channels, discarding crosstalk (Supplementary figure 5).
451 Further discarding unspecific channel bleeding, some cells that exclusively express Spastin-RFP,
452 harbor puncta that are exclusively seen in one channel, as indicated in supplementary figure 5.
453 Similarly, some strong GFP puncta (indicated in the image) are not detected in the RFP channel
454 (Supplementary figure 5). Complementary, cells co-transfected with Rtn-1A-RFP and GFP show
455 distinct distribution patterns without overlapping puncta, supporting that the punctate distribution
456 of GFP is associated exclusively with Spastin co-expression and not explained by unspecific
457 bleeding (Supplementary figure 5).
458
459 Of note, Spastin-RFP pattern was drastically altered when co-expressed with Rtn-1C-
460 GFP (Figure 7B, middle panels). As such, and potentially compatible with their previously
461 reported direct interaction, Spastin closely followed the Rtn-1C pattern distribution (Figure 7B,
462 middle panels). Conversely, Rtn-1A-GFP showed minimal overlap with Spastin-RFP (Figure 7B,
463 lower panels). Quantification of protein colocalization by Mander's coefficients substantiated
464 these observations (Figure 7C).
465
466 Notably, the co-expression of Spastin-RFP with Rtn-1C-GFP maintained tubulin levels
467 unaltered when compared to non-transfected cells from each experimental condition, in marked
468 contrast with their GFP and Rtn-1A-GFP counterpart (Figure 7 B and C). Furthermore, the
469 filamentous distribution of tubulin was clearly preserved with Spastin-RFP/ Rtn-1C-GFP co-
470 expression, which is a strong indicative of limited severing of microtubule filaments (Figure 7 B,
471 middle panels). These effects cannot be attributed to differences in transfection efficiency, as
472 fluorescence intensity of Spastin-RFP and GFP constructs did not significantly differ across
473 conditions (Supplementary figure 5). Therefore, these results suggest that the tight co-distribution
474 of Rtn-1C with Spastin is associated with reduced microtubule severing activity, which is not
475 observed for the Rtn-1A isoform.
476 The examination of the sequences of Rtn-1C and 1A reveals a unique N-terminal variance
477 as the point of differentiation between both isoforms, as they share their RHD region (Figure 7D).
478 Considering the limited colocalization of Rtn-1A with Spastin (Figure 7B, lower panels), RHD
479 appears not to be sufficient for their interaction. This observation hints at the exclusive 20 N-

480 terminal amino acids of Rtn-1C as being critical for Spastin binding. Therefore, we performed *in*
481 *silico* modeling of the Rtn-1C N-terminal and anticipated its affinity with the microtubule-binding
482 domain (MTBD) of Spastin. This domain showed larger interaction energies compared to the
483 endosome (Microtubule Interacting and Trafficking domain, MIT) and microtubule severing
484 domain (ATPases Associated with diverse cellular Activities, AAA) (Figure 7E). Furthermore,
485 the affinity of a Rtn-1A equivalent region for these domains was also less thermodynamically
486 favored compared to Rtn-1C (Figure 7E). These results are compatible with previous evidence
487 showing that deletion of Spastin's MIT domain, and most of the MTBD region, abrogates Spastin-
488 Rtn-1C co-precipitation(Mannan et al., 2006c). This suggests that Rtn-1C binding to Spastin
489 MTBD is competing with the binding of this domain to microtubules. Mechanistically, this would
490 prevent the ring conformation around microtubule filaments required for the severing activity of
491 Spastin(Roll-Mecak & Vale, 2008). Overall, these findings reveal that Rtn-1C, but not Rtn-1A,
492 closely associates with Spastin, leading to a reduction in its microtubule severing activity.
493

494 **Discussion**

495

496 This study uncovers a mechanism whereby downregulation on the local synthesis of an
497 ER-shaping protein promotes the outgrowth of injured cortical axons. Our results support that this
498 enhancement is dependent on the shielding effect that axonally synthesized Rtn-1C exerts over
499 Spastin microtubule severing, and on microtubule dynamics. Using this mechanism, cortical
500 neurons may precisely and locally control outgrowth after injury. This finely tuned response after
501 damage is intriguing given that its halting effect on outgrowth may seem, at first sight, detrimental
502 for proper regeneration. However, we may speculate that limiting microtubule stability in injury
503 site helps axons to accumulate molecular components required for a successful injury repair. In
504 any case, it would be interesting to explore whether local synthesis of Rtn-1 offers a potential
505 therapeutic pathway to enhance regeneration by unleashing the shielding effect of Rtn-1C
506 synthesis over Spastin locally in axons.

507

508 **Control of Rtn-1 synthesis as an adaptive mechanism for axonal injury.**

509 It would also be interesting to further explore whether developing neurons decrease
510 axonal *Rtn-1* mRNA as a mechanism to promote outgrowth during development and after
511 damage. For instance, a previous study using axotomized 10 DIV rat cortical neurons in
512 microfluidic chambers found a decrease on *Rtn-1* mRNA levels compared to non-injured
513 axons(Taylor et al., 2009b). Currently, it is unknown to what extent a similar mechanism is
514 retained in adult cortical neurons. Likewise, we do not know whether this phenomenon is fully
515 operative *in vivo,* even though the mRNA for Rtn-1 is consistently found *in vitro* and *ex vivo*. Of
516 note, *Rtn-1* mRNA is dynamically regulated in the axonal translatome of retinal ganglion cells *in*
517 *vivo*(Shigeoka et al., 2016), but the functional implications of axonal Rtn-1 synthesis in a more
518 physiological context are yet to be elucidated [59]. Interestingly, growing axonal tips from injured
519 nerves in Lamprey are nearly 13-fold enriched in *Spastin* mRNA, suggesting that other constituent
520 of our described mechanism may be locally synthesized after injury(Jin et al., 2022).

521 The presence of the axonal ER (particularly the smooth ER) is thought to be critical for
522 promoting the regeneration of injured neurites by providing membranes and controlling calcium
523 and microtubule dynamics required for outgrowth (Luarte et al., 2018b). This has been supported
524 by evidence showing the distribution of smooth ER markers, including ER-shaping proteins such
525 as Reticulons, REEPs, Atlastin, and Spastin isoforms, preferentially at the distal tip of
526 regenerating neurites (Rao et al., 2016c; Stone et al., 2012b). Indeed, Reticulons share RHD with
527 REEPs, some Spastin isoforms, and atlastins, which makes them suitable to shape the mostly
528 tubular smooth ER (Chiurchiù et al., 2014; Iwahashi et al., 2007). Highlighting their functional
529 relevance, forcing the localization of smooth ER into axonal tips by the over-expression of the

530 ER membrane protein protrudin enhances outgrowth of CNS axons(Petrova et al., 2020) .
531 Different studies have shown that the presence of the axonal ER is associated with the fine-tuning
532 of microtubules stability required for outgrowth (Farías et al., 2019b; Lee et al., 2009; Rao et al.,
533 2016d). Our results support a model where axonal outgrowth after injury is restricted by reducing
534 the microtubule growth processivity controlled by locally synthesized Rtn-1C. As such, axonal
535 KD of *Rtn-1C* mRNA may set an optimal range of microtubules dynamicity, resembling the
536 beneficial role observed with the treatment of low-dose microtubule stabilizers in axonal
537 regeneration(Brizuela et al., 2015; B. Liu et al., 2023). These results would explain why we
538 observed pronounced trend (yet non-significant) of SPTZ to increase regeneration when applied
539 alone locally in axons (Figure 5C-D). The opposite trend of SPTZ treatment alone with the less-
540 regenerating condition (SPTZ+ Rtn-1 siRNA) highlights the specificity of this response, pointing
541 that microtubule dynamics have relatively narrow optimal range to promote outgrowth
542 (Sengottuvel et al., 2011).

543 The differential injury response in axonal outgrowth observed after somatic or axonal
544 Rtn-1 KD, emphasizes the unique molecular and structural environments of axons versus cell
545 bodies. This difference might be explained by at least two scenarios. Firstly, we used a Rtn-1
546 siRNA that is directed against the conserved RHD sequence; thus, it also targets the Rtn-1A
547 isoform. For instance, we observed limited co-distribution of Rtn-1A with Spastin compared to
548 Rtn-1C, and its N- terminal recruits other signaling pathways (Kaya et al., 2013). Therefore, the
549 observed differential response might be due to the predominant presence of Rtn-1C in axons,
550 while both isoforms are present in the cell bodies. Secondly, increased microtubule severing after
551 axonal Rtn-1 KD might promote outgrowth when coupled to predominantly outward-directed
552 growing filaments that characterize axons, but not with the radial or mixed orientation of
553 microtubules in the cell bodies and dendrites(Baas et al., 2016).

554 **The role of Spastin's microtubule severing on outgrowth after injury**

555 The positive relationship that we observed between increased Spastin-severing activity
556 and the outgrowth of injured axons may seem counter-intuitive. However, microtubule severases,
557 such as Spastin or Katanin, are known to increase microtubule mass and growth processivity
558 under certain conditions. Indeed, Spastin can stabilize newly produced microtubule tips,
559 paradoxically yielding a net increase in microtubule mass(Kuo & Howard, 2021). Furthermore,
560 Spastin tends to concentrate at the tip of growing microtubules to behave as a dual enzyme that
561 cleaves but also stabilizes them after cutting (Kuo et al., 2019b). This may also partially explain
562 why we observed that the axonal inhibition of Spastin by SPTZ alone tends to promote outgrowth
563 after injury (Figure 5C-D).

564 Collectively, our results are compatible with axonal Rtn-1 KD releasing Spastin
565 molecules to sever more microtubules, and thus, promote a net increase on growing ends and
566 potentially filament mass. It remains to be solved whether this potential increase in microtubule
567 mass improves the efficacy of elongation that we observed with axonal Rtn-1 KD after injury. In
568 agreement with this speculation, inhibition of axonal tyrosine ligase (which favor dynamic
569 microtubule ends) impedes outgrowth in injured axons from dorsal root ganglion(Song et al.,
570 2015). Analogously, when Fidgetin (a severing enzyme of microtubule labile ends) is depleted in
571 neurons, axonal regeneration is improved(Matamoros et al., 2019).

572 Like other studies, we observed that increased axonal outgrowth correlates with dynamic
573 microtubule parameters such as growth rate(Liz et al., 2014). However, others have shown that
574 the dynamic properties of microtubules, including microtubule growth rate and track length, can
575 adapt to different outgrowth scenarios, with low capacity to predict axonal extension (Kiss et al.,
576 2018). Thus, controlling dynamic parameters of microtubules is not the only factor that
577 determines the outgrowth capacity of injured axons. The exact mechanisms by which locally
578 synthesized Rtn-1C controls dynamic parameters of microtubules remains unsolved. Other
579 Spastin-independent interactions of Rtn-1 may depend on its presence on the tubular ER, which
580 includes the control of functional contacts with mitochondria and autophagosomes (D' Eletto et
581 al., 2019; Reali et al., 2015), but their implications for microtubule dynamic parameters and
582 axonal extension also remain to be solved.

583 Decreasing axonal Rtn-1C translation or increasing Spastin microtubule severing locally
584 in axons may constitute emerging mechanism for promoting injury recovery. For instance, local
585 application of recombinant Spastin together with polyethylene glycol increases recovery after
586 sciatic nerve injury (Y. F. Lin et al., 2019). Furthermore, local augmentation of axonal Spastin by
587 the pharmacological local regulation of 14-3-3 promotes the recovery of spinal cord injury(Q. Liu
588 et al., 2024) . Indeed, axonal regeneration is particularly sensitive to the absence of Spastin(Stone
589 et al., 2012c). Similarly, results in drosophila show that Spastin gene dosage is particularly
590 relevant for the regenerative response of axons (Stone et al., 2012d) .

591 **Implications for length-dependent axonopathies and injury response**

592 The failure of ER shaping protein-function potentially participates in the etiology of
593 multiple length-dependent axonopathies such as hereditary spastic paraplegias (HSPs)
594 (Blackstone et al., 2011). Here, we have described a relevant role relating Rtn-1C with Spastin,
595 which is the most frequently mutated isoform in HSP (Hazan et al., 1999; Mannan et al., 2006c).
596 As a second point of analysis, most of the studies performed to understand axonopathies and
597 axonal damage have focused on a "cell-body-centered view" for protein synthesis and ER
598 function. However, increasing evidence supports the relevance of axonal autonomous response to

599 injury or cues from the local brain microenvironment (Jung et al., 2014; Lopez-Verrilli et al.,
600 2013; Zhang et al., 2013b, 2015). Similarly, our work underscores a highly local injury adaptation,
601 which is in harmony with the astonishing extension of central nervous system's axons (H.-M. Lin
602 et al., 2018). These results may provide understanding of axonal pathologies and injury response
603 with a special focus on the autonomous response of cortical axons.

604

605 **Materials and Methods**

606

607 **Animals and surgical procedures.** Pregnant Sprague–Dawley rats at embryonic day 18 were
608 obtained from the Central Animal Facility of Universidad Católica de Chile and euthanized in
609 accordance with the guidelines of the Agencia Nacional de Investigación y Desarrollo de Chile
610 (ANID). All experimental procedures were approved by the Institutional Bioethics Committee of
611 Universidad de los Andes (CEC2022106).

612

613 **Neuron cell cultures.** Cortical neurons were cultured from 18-day embryos like previously
614 reported (Deitch & Banker, 1993b). Dissociated primary cortical neurons (20,000-30,000 cells)
615 were seeded on glass coverslips coated with 0.1 mg/mL poly-L-lysine (Sigma-Aldrich, P4707).
616 Microfluidic chambers were prepared as previously reported (Taylor et al., 2005). Chambers
617 harboring axonal and somatic compartment connected with 750 μm long microgrooves were
618 mounted over a squared 25mm glass coverslip previously coated with 0.1 mg/mL poly-D-lysine
619 (Corning, 354210) and 2 μg/mL laminin (Sigma, L2020). Plating medium was completely
620 replaced with growth medium 24 hours after seeding. Plating medium contained MEM (Gibco,
621 15630080), 10 % horse serum (Gibco, 16050122), 0.6 % D-glucose (Sigma Aldrich, G8769), 0.1
622 % Glutamax (Gibco, 35050061), 2 % penicillin/ 0.1 % streptomycin (Life
623 Technologies,15140122), while growth medium contained Neurobasal (Gibco, 21103049), 3 %
624 B27 (Gibco, 17504044), 0.1 % Glutamax, penicillin/streptomycin 0.1 %). 100 μL of fresh growth
625 medium was added with a frequency of 48 hours to the somatic compartment to prevent loss of
626 water. Neuron ball cell culture was performed as previously reported (Sasaki et al., 2010).Neurons
627 were suspended on growth medium supplemented with 10 % horse serum. A total amount of
628 30,000 cells was seeded as hanging drops of 20 μL during 3 days inside the cover of 100 mm
629 dishes filled with water. Floating spheres were gently washed three times to discard non-attached
630 cells and then seeded on poly-L-lysine coated culture plates. Each well contained 400 μL of
631 growth medium previously supplemented with 1 μM cytosine *β*-d-arabinofuranoside
632 hydrochloride (AraC, Sigma-Aldrich, C1768) to prevent glial growth. Neurites were allowed to
633 grow until 7 days after seeding. The periphery of each neuron ball was carefully scraped with a
634 pipette and washed three times with cold PBS to further remove any remaining cell bodies. Cell-
635 body-containing spheres were extracted by vacuum suction.

636

637 **Immunofluorescence.** Cells were washed twice with PBS and fixed with 4% PFA (Sigma
638 Aldrich, P6148) and 4% sucrose for 20 min at room temperature. The same procedure was applied
639 to COS-7 cells. For assessment of growth cone morphology, neurons were fixed for 20 min at
640 room temperature by adding an equal volume of 8% PFA and 22% sucrose in PBS directly to the
641 culture medium. After fixation, cells were washed twice with PBS and sequentially incubated for
642 10 min each at room temperature with: (i) permeabilization solution (0.5% NP-40 [Abcam,
643 ab142227] and 0.5% w/v Bovine Serum Albumin [Winkler, BM-0150] in PBS); (ii) quenching
644 solution (50 mM NH_4Cl in PBS); and (iii) blocking solution (0.5% w/v Bovine Serum Albumin
645 and 5% Fetal Bovine Serum [Sigma Aldrich, F2442] in PBS).Primary antibodies, diluted in 0.5%
646 w/v Bovine Serum Albumin in PBS, were incubated overnight at 4 °C. Coverslips were then
647 washed three times (5 min each) with the same solution and incubated with secondary antibodies,
648 diluted in the same buffer, for 1 h at room temperature. Finally, samples were washed with PBS
649 and distilled water and mounted using VECTASHIELD®.

650

651 **Colocalization analysis**. COS-7 cells were transfected with indicated plasmids for twenty-four
652 hours and imaged using a confocal microscope (Fluoview FV1000, Olympus) equipped with a
653 UPLSAPO 60×/1.35 NA objective and 4× digital zoom. Images were acquired with a Kalman
654 filter (two iterations). For each condition, an average of 8–12 confocal sections (0.2 µm thickness
655 each) were analyzed per cell. Colocalization between RFP and GFP signals was quantified using
656 Manders' coefficients (M1 and M2) with the JaCoP plugin (Just Another Colocalization Plugin)
657 in ImageJ (FIJI). Identical thresholding parameters were applied to each channel across all
658 conditions.

659 **Fluorescence intensity analysis of COS-7.** COS-7 cells were imaged with a Leica TCS SP8
660 confocal microscope using a 40×/1.30 NA oil-immersion objective. For each field, z-stacks of
661 15–17 optical sections (1 µm step size) were acquired, and summed intensity projections were
662 generated for analysis. Acquisition parameters (laser power, detector gain, and offset) were kept
663 constant across all conditions. Cells were manually segmented in FIJI using α-tubulin
664 immunostaining to delineate them. For each ROI, mean fluorescence intensity of β3-tubulin, GFP,
665 and RFP channels was measured, and background signal (from a cell-free region of the same
666 image) was subtracted. Corrected mean intensity was multiplied by the soma area to calculate
667 total fluorescence per cell. Fold change values were obtained by normalizing to the mean of the
668 control group.

669 **Fluorescence intensity analysis of somas and axons.** Images were acquired using an Olympus
670 BX61WI microscope in wide-field configuration equipped with a 40×/1.30 NA oil-immersion
671 objective and a Hamamatsu ORCA-R2 CCD camera, controlled by Cell^R software (Olympus,
672 Tokyo, Japan). Exposure time, gain, binning, and illumination settings were kept constant across

673 all conditions. For somatic quantifications, cell bodies were manually segmented in FIJI using
674 β3-tubulin staining as a guide, restricting the region of interest (ROI) to the soma and excluding
675 processes. For each cell, the mean background intensity (measured in a cell-free region of the
676 same image) was subtracted from the mean somatic intensity, and total fluorescence was
677 calculated. Fold change per cell was determined by normalizing to the mean value of the control
678 group. For axonal quantification a 1-µm-wide segmented line was drawn starting at the axon tip
679 and extending 50 µm proximally to extract the intensity profile (FIJI). Background intensity was
680 subtracted from each profile using values measured in axon-free areas of the same image. For
681 quantifying protein changes, the integrated intensity across the entire 0–50 µm segment was
682 calculated and expressed as fold change relative to controls. To visualize profiles for β3-tubulin,
683 a per-axon baseline was additionally set by subtracting the intensity at 0 µm (the tip) from the
684 entire profile (corrected intensity). To obtain the corrected intensity of Rtn-1, the average pixel
685 intensity within the last 5 µm of the profile (45–50 µm from the tip) was subtracted from the
686 entire trace of each axon. The corrected integrated intensity over 0–50 µm was then normalized
687 to the control group mean to obtain fold change values. These normalizations were applied
688 exclusively for plotting purposes and not for fold change calculations.
689
690 **Stimulated emission depletion (STED) super resolution microscopy analysis of axons**
691 Super-resolution imaging was performed on TCS SP8-3X STED microscope system (Leica
692 Microsystems) equipped with a HC APO CS2 100x/1.40 oil objective. Distal axons of
693 microfluidic chambers were imaged using excitation and depletion laser lines appropriate for each
694 fluorophore (see Reagents in supplementary material). Images were digitalized in 1024 × 1024
695 pixels format file with 5x zoom factor. These settings achieved 18.93 nm resolution in the XY
696 axis and a 220 nm resolution in Z. Four confocal slices from each axons were analyzed. To prevent
697 the introduction of potential artifacts that could distort the previously uncharacterized distribution
698 of Spastin in growth cones, no deconvolution or post-processing algorithms were applied. Instead,
699 all quantitative and qualitative analyses were performed directly on the raw STED images.
700 Acquisition parameters (laser power, detector gain, pixel size, and dwell time) were kept constant
701 across conditions. For quantification, the total fluorescence intensity of the last 15 µm of each
702 distal axon was measured after background subtraction. Two analyses were performed: (i)
703 intensity fold change was calculated by comparing non-axotomized and axotomized axons; and
704 (ii) the corrected intensity of each channel was divided by the total intensity across channels to
705 obtain the relative distribution of fluorescence.
706
707 **Transfections.** All transfections were performed with lipofectamine 3000 (Thermo Fisher,
708 L3000001) following manufacturer's instructions but without using p3000 reagent. For neurons
709 and COS-7 cells, RNA or DNA complexes were added to chambers diluted on Neurobasal

710 medium to a total volume of 50 µL per microfluidic chambers or 100 µL for 12mm coverslips.
711 For axonal transfection of siRNAs, medium on the axonal compartment was carefully removed
712 and replaced with 50 µL of the transfection mixture containing 20 pmol of the corresponding
713 oligonucleotide plus 50 µL of fresh growth media. Near 300 µL of conditioned medium remained
714 at the somatic compartment, generating positive flux towards the axons. By the opposite, for
715 somatic transfection the medium present at the somatic compartment was carefully removed and
716 replaced with 50 µL of the transfection mixture plus 100 µL of fresh growth media, this time
717 generating positive flux towards the soma. For validating siRNA efficiency, 200,000 neurons
718 were seeded on 35 mm plates and transfected with 40 pmol of corresponding oligos and submitted
719 to western blot after forty-eight hours. For colocalization, Western blot, and immunofluorescence
720 analyses, COS-7 cells were seeded at ~1–2 × 10^5 per 25 mm coverslip and cultured for 24 h before
721 transfection with 500 ng of pCMV3-C-GFPSpark plasmid encoding either Rtn-1C-GFP or Rtn-
722 1A-GFP, together with pCMV3-C-ORFSpark encoding Spastin-RFP (all plasmids are detailed in
723 the Reagents section of the Supplementary Figures).
724
725 **Axotomy and Sholl analysis.** At 8 DIV, axons were removed from the axonal compartment of
726 microfluidic chambers by vacuum aspiration performed five times with 100 µL of pure
727 Neurobasal medium. Subsequently, all media was removed, and the transfection mixture was
728 added either to the axonal or somatic compartment. For quantification of axonal outgrowth,
729 images of β3-tubulin–stained axons were binarized and manually segmented to fully trace axonal
730 trajectories. Sholl analysis was performed in FIJI using the Neuroanatomy plugin, applying
731 concentric semi-circles at 2 µm radial intervals starting from the center of microgroove until 1200
732 or 1500 µm final distance.
733
734 **Probe-labeling of primary antibodies for puromycilation proximity ligation assay (puro-**
735 **PLA).** Monoclonal antibodies mouse anti-Reticulon-1C and mouse anti-puromycin (3RH1,
736 Kerafast) were directly labeled with the Duolink® in Situ Probemaker PLUS (1002748995, Sigma
737 Aldrich) and MINUS (1002748992, Sigma Aldrich), respectively, following manufacturer`s
738 instructions. Both antibodies with a concentration of 1 µg/µL were labeled overnight at room
739 temperature with the corresponding buffer and probes to a final volume of 20 µL. Labeled
740 antibodies were further diluted with 20 µL of storage solution.
741
742 **Puro-PLA staining protocol.** Puro-PLA was performed on similar conditions to well stablished
743 protocols (Dieck et al., 2015). Briefly, a 15-min pulse of 1.8 µM puromycin (P8833, Sigma-
744 Aldrich) was applied exclusively to the axonal or somatic compartment of microfluidic chambers
745 containing 9 DIV cortical neurons. As an additional control, this incubation was performed after

746 90 min of local pretreatment with 40 nM emetine (E2375, Sigma-Aldrich) in distilled water
747 (vehicle), added either to the somatic or axonal compartment to block protein synthesis.
748 Immediately after incubations, cells were washed twice with PBS and fixed with 4%
749 paraformaldehyde and 4% sucrose in PBS for 20 min at room temperature, followed by three PBS
750 washes (5 min each). Cells were then permeabilized with 0.25% Triton X-100 in PBS for 10 min,
751 washed three times with PBS (5 min each), blocked with 5% goat serum in PBS for 1 h, and
752 incubated overnight at 4 °C with probe-labeled antibodies (anti–Reticulon-1C, 1:50; anti-
753 puromycin, 1:200) diluted in the same blocking solution. Detection of locally synthesized
754 Reticulon-1C was performed following the manufacturer's instructions, except that no labeled
755 secondary antibody step was included. Afterward, cells were incubated for 1 h at room
756 temperature with anti-β3-tubulin conjugated to Alexa Fluor 488, and mounted with Duolink In
757 Situ Mounting Medium with DAPI (Sigma-Aldrich). Images were acquired as previously
758 described using a Zeiss LSM 800 confocal microscope with a 63× oil objective. PLA-positive
759 puncta present within a β3-tubulin mask were quantified using FIJI software.
760
761 **RT-PCR.** For axonal RNA isolation, at least 200 neuron balls were desomatized and processed
762 using the lysis buffer provided in the RNAqueous™-Micro Total RNA Isolation Kit (AM193,
763 Thermo Fisher), following the manufacturer's instructions. Total RNA was eluted twice to a final
764 volume of 30 µL. Approximately 20–30 axotomized neuron balls were processed using the same
765 protocol, and the RNA was resuspended in 30 µL.Reverse transcription was performed with 100
766 ng of RNA as input using the High-Capacity cDNA Reverse Transcription Kit (4368814, Thermo
767 Fisher). Resulting cDNA products were treated with DNase according to the manufacturer's
768 instructions (EN0521, Thermo Fisher). For PCR, 3 µL of cDNA was amplified using GoTaq®
769 Green Master Mix, 2X (M712, Promega), with the following cycling parameters: initial
770 denaturation at 95 °C for 5 min; 35 cycles of denaturation at 95 °C for 30 s, annealing at 57 °C
771 for 30 s, and extension at 72 °C for 45 s; followed by a final extension at 72 °C for 10 min.PCR
772 products (10 µL) were loaded on a 2% agarose gel and stained with GelRed® Nucleic Acid Gel
773 Stain (Biotium, 41003), following the manufacturer's recommendations.
774
775 **Western blot.** Proteins were isolated using RIPA buffer (50 mM Tris-HCl, pH 7.4, 150 mM
776 NaCl, 0.25% deoxycholic acid, 1% NP-40, 1% SDS, 1 mM EDTA) supplemented with protease
777 and phosphatase inhibitors (Thermo Fisher, A32963). Extracted proteins were quantified using
778 the Bicinchoninic Acid (BCA) method (Thermo Fisher, 23225) and separated on polyacrylamide
779 gels under denaturing conditions (SDS-PAGE; Cleveland et al., 1977). For each sample, 20 µg of
780 protein was loaded per lane for both complete neuronal or cell homogenates and axonal or somatic
781 fractions of neuron balls. Proteins were resolved on 15% linear acrylamide gels by electrophoresis
782 at 70 V for 45 min followed by 100 V for 45 min. Gels were transferred to nitrocellulose

783 membranes (Bio-Rad) at a constant current of 350 mA for 90 min. After transfer, membranes
784 were blocked with 5% (w/v) skim milk in PBS for one hour at room temperature under constant
785 agitation and then incubated overnight at 4 °C with the corresponding primary antibody diluted
786 in PBS. The following day, membranes were incubated with the appropriate secondary antibody
787 for one hour at room temperature. When indicated, total protein loading was normalized using
788 No-Stain™ total protein labeling reagent (Thermo Fisher, A44449) according to the
789 manufacturer's instructions. Bands and lanes were quantified by densitometry using Photoshop
790 7.0 (Adobe).
791 **Live imaging of microtubule plus-ends.** Neurons were cultured in microfluidic chambers and
792 transfected with EB3-Emerald GFP plasmid at 7 DIV. At 8 DIV, neurons were axotomized by
793 vacuum aspiration, and siRNAs were delivered into the axonal compartment. Forty-four hours
794 later, axons were imaged. The Spastin inhibitor Spastazoline (HY-111548, MedChemExpress)
795 was added to the axonal compartment 4–5 h after axotomy and siRNA transfection at a final
796 concentration of 50 nM.For live imaging, EB3-Emerald–transfected axons were randomly
797 selected and imaged in Tyrode's solution (125 mM NaCl, 2 mM KCl, 2 mM $CaCl_2$, 2 mM $MgCl_2$,
798 30 mM glucose, 25 mM HEPES, pH 7.4) at 32 °C. Cells were equilibrated for 10 min before
799 recording. Movies were acquired for 3 min at 2 frames/s. To maintain hydrostatic pressure
800 towards the axonal side, the volume difference between compartments was carefully preserved
801 throughout the experiment. Imaging was performed on an inverted microscope (Observer.D1,
802 Zeiss) equipped with an EMCCD camera (Evolve 512, Photometrics) controlled by VisiView®
803 software (Visitron Systems GmbH). A 63× oil-immersion objective and a GFP single-band
804 exciter ET filter set (excitation 470/40, emission 59022m, dichroic 59022BS) were used. The
805 mEmerald-EB3-C-20 plasmid was a gift from Michael Davidson (Addgene plasmid #54076;
806 http://n2t.net/addgene:54076; RRID: Addgene_54076).
807
808 **Analysis of microtubule dynamics.** All acquired time series were filtered using the Gaussian
809 Blur 3D function in FIJI. Mobile components of the series were isolated by applying a 4-sigma
810 Gaussian blur, while more static elements were extracted by applying a 50-sigma blur. To enhance
811 detection of moving structures, static components were subtracted from mobile components using
812 the *Image Calculator* function in FIJI. The resulting filtered image series were then used to
813 generate kymographs with the FIJI plugin *Kymograph Builder*. Kymographs were constructed
814 from the distal portion of axons by tracing a 1-µm-wide line, with a total length ranging from 30
815 to 50 µm. Growth cones were excluded from the analysis. All analyzed parameters were
816 quantified as previously described. (Stepanova et al., 2010). EB3-Emerald comets were analyzed
817 from kymographs in FIJI. Individual dashes corresponding to microtubule growth events were
818 manually traced using the Segmented Line tool. The angle of each dash was measured relative to
819 the x-axis. The horizontal projection of the dash, obtained by multiplying its length by the cosine

820 of the angle, was considered as the track length and represents the distance traveled by the comet
821 in micrometers. The vertical projection, obtained by multiplying the dash length by the sine of
822 the angle, was proportional to comet lifetime. To obtain comet lifetime in seconds the calculated
823 vertical projection was divided by the total y-axis length of the recording kymograph and
824 multiplied by the total acquisition time (180 seconds for a 3-minute movie). Growth speed was
825 calculated by dividing the track length by the comet lifetime for each dash. Only dashes traceable
826 across at least two consecutive frames were included in the analysis.
827 **Molecular docking between Spastin (M87) and Rtn-1C**. Firstly, Spastin M87 and Rtn-1A
828 models of rattus norvegicus were retrieved from AlphaFold Protein Structure Database (accession
829 numbers AF-A0A0G2K590 and AF-Q64548, respectively). Then, M87 spastin model were
830 generated from the removal of the first 86 amino acids of the M1 Spastin model, whereas Rtn-1C
831 3D-structure was built with MODELLER version 10.4 using Rtn-1A model as template. For this,
832 amino acid sequences of Rtn-1C were retrieved from UniprotKB/Swissprot (accession numbers
833 Q64548). Additionally, the first 20 amino acids (of the N-terminal region) of the Rtn-1C model
834 and region 200-317 containing the microtubule-binding domain of Spastin M87 were refined
835 using ModLoop server (Fiser & Sali, 2003). Subsequently, we evaluated the interaction of the
836 Rtn-1C N-terminal with three domains of Spastin M87- endosome o MIT (region 116-194),
837 microtubule-binding (region 270-328) and microtubule-severing o AAA ATPase (region 342-
838 599) - using the HADDOCK docking protein-protein web server (Van Zundert et al., 2016).
839 Among many models, low-energy conformations for each complex were extracted from
840 HADDOCK 2.2 server, as previously described (Acevedo et al., 2018) The binding energy (ΔG_{bin})
841 of the complexes were predicted using the PRODIGY web server at temperature of 310 K, and
842 chains identifiers for Rtn-1 and Spastin M87 were specified as Interactor 1 and 2, respectively.
843 Finally, graphical analysis of molecular docking studies was performed using VMD 1.9.2
844 software (Humphrey et al., 1996) .
845
846 **Statistical Analysis.** Unless otherwise stated, data are presented as mean ± standard error.
847 Normality was assessed using the Shapiro–Wilk test. For normally distributed data, comparisons
848 between two groups were performed using two-tailed Student's t-test; for non-normally
849 distributed data, the two-tailed Mann–Whitney *U t*est was applied. Western blot fold change
850 values were compared to a theoretical mean of 1 using the Wilcoxon signed-rank test. For
851 comparisons among multiple groups, one-way ANOVA followed by Tukey's post hoc test was
852 used for normally distributed data, whereas the Kruskal–Wallis test followed by Dunn's post hoc
853 test was applied for non-parametric data. Statistical significance was defined as $p < 0.05$.
854 Fluorescence intensity experiments in Figures 2 and 4 were analyzed at the single-cell level using
855 linear mixed-effects (LME) models, with experimental date included as a random effect.

Statistical tests were performed using GraphPad Prism (GraphPad Software, San Diego, CA, USA) and R (v4.0 or later) with the lme4 and lmerTest packages.

References

Acevedo, W., Ramírez-Sarmiento, C. A., & Agosin, E. (2018). Identifying the interactions between natural, non-caloric sweeteners and the human sweet receptor by molecular docking. *Food Chemistry*, *264*, 164–171. https://doi.org/10.1016/J.FOODCHEM.2018.04.113

Aiken, J., & Holzbaur, E. L. F. (2024). Spastin locally amplifies microtubule dynamics to pattern the axon for presynaptic cargo delivery. *BioRxiv*, *123*(3), 332a. https://doi.org/10.1101/2023.08.08.552320

Allison, R., Edgar, J. R., & Reid, E. (2019). Spastin MIT Domain Disease-Associated Mutations Disrupt Lysosomal Function. *Frontiers in Neuroscience*, *13*, 486039. https://doi.org/10.3389/FNINS.2019.01179/BIBTEX

Allison, R., Lumb, J. H., Fassier, C., Connell, J. W., Martin, D. Ten, Seaman, M. N. J., Hazan, J., & Reid, E. (2013). An ESCRT-spastin interaction promotes fission of recycling tubules from the endosome. *Journal of Cell Biology*, *202*(3), 527–543. https://doi.org/10.1083/JCB.201211045/VIDEO-2

Aridor, M., & Fish, K. N. (2009). Selective Targeting of ER Exit Sites Supports Axon Development. *Traffic*, *10*(11), 1669–1684. https://doi.org/10.1111/j.1600-0854.2009.00974.x

Baas, P. W., Rao, A. N., Matamoros, A. J., & Leo, L. (2016). Stability properties of neuronal microtubules. *Cytoskeleton (Hoboken, N.J.)*, *73*(9), 442. https://doi.org/10.1002/CM.21286

Baleriola, J., Walker, C. A., Jean, Y. Y., Crary, J. F., Troy, C. M., Nagy, P. L., & Hengst, U. (2014). Axonally synthesized ATF4 transmits a neurodegenerative signal across brain regions. *Cell*, *158*(5), 1159–1172. https://doi.org/10.1016/J.CELL.2014.07.001

Batista, A. F. R., Martínez, J. C., & Hengst, U. (2017). Intra-axonal Synthesis of SNAP25 Is Required for the Formation of Presynaptic Terminals. *Cell Reports*. https://doi.org/10.1016/j.celrep.2017.08.097

Bigler, R. L., Kamande, J. W., Dumitru, R., Niedringhaus, M., & Taylor, A. M. (2017). Messenger RNAs localized to distal projections of human stem cell derived neurons. *Scientific Reports 2017 7:1*, *7*(1), 1–11. https://doi.org/10.1038/s41598-017-00676-w

Blackstone, C., Kane, C. J. O., Reid, E., O'Kane, C. J., & Reid, E. (2011). Hereditary spastic paraplegias: membrane traffic and the motor pathway. *Nature Reviews. Neuroscience*, *12*(1), 31–42. https://doi.org/10.1038/nrn2946

Brizuela, M., Blizzard, C. A., Chuckowree, J. A., Dawkins, E., Gasperini, R. J., Young, K. M., & Dickson, T. C. (2015). The microtubule-stabilizing drug Epothilone D increases axonal sprouting following transection injury in vitro. *Molecular and Cellular Neuroscience*, *66*(PB), 129–140. https://doi.org/10.1016/j.mcn.2015.02.006

Chiurchiù, V., Maccarrone, M., & Orlacchio, A. (2014). The role of reticulons in neurodegenerative diseases. *Neuromolecular Medicine*, *16*(1), 3–15. https://doi.org/10.1007/s12017-013-8271-9

Cooke, P., Janowitz, H., & Dougherty, S. E. (2022). Neuronal Redevelopment and the Regeneration of Neuromodulatory Axons in the Adult Mammalian Central Nervous System. *Frontiers in Cellular Neuroscience*, *16*, 872501. https://doi.org/10.3389/FNCEL.2022.872501/BIBTEX

Cornejo, V. H., Luarte, A., & Couve, A. (2017). Global and local mechanisms sustain axonal proteostasis of transmembrane proteins. *Traffic*, *18*(5), 255–266. https://doi.org/10.1111/tra.12472

Cupido, T., Pisa, R., Kelley, M. E., & Kapoor, T. M. (2019). Designing a chemical inhibitor of the AAA protein spastin using active site mutations. *Nature Chemical Biology*, *15*(5), 444. https://doi.org/10.1038/S41589-019-0225-6

D' Eletto, M., Risuglia, A., Oliverio, S., Mehdawy, B., Nardacci, R., Bordi, M., & Di Sano, F. (2019). Modulation of autophagy by RTN-1C: role in autophagosome biogenesis. *Cell Death & Disease*, *10*(12). https://doi.org/10.1038/S41419-019-2099-7

de Juan-Sanz, J., Holt, G. T., Schreiter, E. R., de Juan, F., Kim, D. S., & Ryan, T. A. (2017). Axonal Endoplasmic Reticulum Ca2+ Content Controls Release Probability in CNS Nerve Terminals. *Neuron*, *93*(4), 867-881.e6. https://doi.org/10.1016/J.NEURON.2017.01.010

Deitch, J. S., & Banker, G. A. (1993a). An electron microscopic analysis of hippocampal neurons developing in culture: early stages in the emergence of polarity. *The Journal of Neuroscience : The Official Journal of the Society for Neuroscience*, *13*(10), 4301–4315. https://doi.org/10.1523/jneurosci.1544-09.2009

Deitch, J. S., & Banker, G. A. (1993b). An electron microscopic analysis of hippocampal neurons developing in culture: early stages in the emergence of polarity. *The Journal of Neuroscience : The Official Journal of the Society for Neuroscience*, *13*(10), 4301–4315. https://doi.org/10.1523/jneurosci.1544-09.2009

Dieck, S. tom, Kochen, L., Hanus, C., Bartnik, I., Nassim-Assir, B., Merk, K., Mosler, T., Garg, S., Bunse, S., Tirrell, D. A., & Schuman, E. M. (2015). Direct visualization of identified and newly synthesized proteins in situ. *Nature Methods*. https://doi.org/10.1038/nmeth.3319

Evans, K., Keller, C., Pavur, K., Glasgow, K., Conn, B., & Lauring, B. (2006). Interaction of two hereditary spastic paraplegia gene products, spastin and atlastin, suggests a common pathway for axonal maintenance. *Proceedings of the National Academy of Sciences of the United States of America*. https://doi.org/10.1073/pnas.0510863103

Farías, G. G., Fréal, A., Tortosa, E., Stucchi, R., Pan, X., Portegies, S., Will, L., Altelaar, M., & Hoogenraad, C. C. (2019a). Feedback-Driven Mechanisms between Microtubules and the Endoplasmic Reticulum Instruct Neuronal Polarity. *Neuron*. https://doi.org/10.1016/j.neuron.2019.01.030

Farías, G. G., Fréal, A., Tortosa, E., Stucchi, R., Pan, X., Portegies, S., Will, L., Altelaar, M., & Hoogenraad, C. C. (2019b). Feedback-Driven Mechanisms between Microtubules and the Endoplasmic Reticulum Instruct Neuronal Polarity. *Neuron*. https://doi.org/10.1016/j.neuron.2019.01.030

Farias, J., Holt, C. E., Sotelo, J. R., & Sotelo-Silveira, J. R. (2020). Axon microdissection and transcriptome profiling reveals the in vivo RNA content of fully differentiated myelinated motor axons. *RNA (New York, N.Y.)*, *26*(5), 595–612. https://doi.org/10.1261/RNA.073700.119

González, C., Cánovas, J., Fresno, J., Couve, E., Court, F. A., & Couve, A. (2016). Axons provide the secretory machinery for trafficking of voltage-gated sodium channels in peripheral nerve. *Proceedings of the National Academy of Sciences of the United States of America*, *113*(7), 1823–1828. https://doi.org/10.1073/PNAS.1514943113

Gumy, L. F., Yeo, G. S. H., Tung, Y. C. L., Zivraj, K. H., Willis, D., Coppola, G., Lam, B. Y. H., Twiss, J. L., Holt, C. E., & Fawcett, J. W. (2011). Transcriptome analysis of embryonic and adult sensory axons reveals changes in mRNA repertoire localization. *RNA (New York, N.Y.)*, *17*(1), 85–98. https://doi.org/10.1261/RNA.2386111

Hazan, J., Fonknechten, N., Mavel, D., Paternotte, C., Samson, D., Artiguenave, F., Davoine, C.-S., Cruaud, C., Dürr, A., Wincker, P., Brottier, P., Cattolico, L., Barbe, V., Burgunder, J.-M., Prud'homme, J.-F., Brice, A., Fontaine, B., Heilig, R., & Weissenbach, J. (1999). Spastin, a new AAA protein, is altered in the most frequent form of autosomal dominant spastic paraplegia. *Nature Genetics*, *23*(3), 296–303. https://doi.org/10.1038/15472

He, Z., & Jin, Y. (2016). Intrinsic Control of Axon Regeneration. *Neuron*, *90*(3), 437–451. https://doi.org/10.1016/J.NEURON.2016.04.022

Humphrey, W., Dalke, A., & Schulten, K. (1996). VMD: Visual molecular dynamics. *Journal of Molecular Graphics*, *14*(1), 33–38. https://doi.org/10.1016/0263-7855(96)00018-5

Iwahashi, J., Hamada, N., & Watanabe, H. (2007). Two hydrophobic segments of the RTN1 family determine the ER localization and retention. *Biochemical and Biophysical Research Communications*, *355*(2), 508–512. https://doi.org/10.1016/j.bbrc.2007.02.001

Jin, L. Q., Zhou, Y., Li, Y. S., Zhang, G., Hu, J., & Selzer, M. E. (2022). Transcriptomes of Injured Lamprey Axon Tips: Single-Cell RNA-Seq Suggests Differential Involvement of MAPK Signaling Pathways in Axon Retraction and Regeneration after Spinal Cord Injury. *Cells*, *11*(15), 2320. https://doi.org/10.3390/CELLS11152320/S1

Jung, H., Gkogkas, C. G., Sonenberg, N., & Holt, C. E. (2014). Remote control of gene function by local translation. In *Cell*. https://doi.org/10.1016/j.cell.2014.03.005

Kaethner, R. J., & Stuermer, C. A. 0. (1992). Dynamics of Terminal Arbor Formation and Target Approach of Retinotectal Axons in Living Zebrafish Embryos: A Time-Lapse Study of Single Axons. *The Journal of Neuroscience*, *72*(8), 32573271.

Kaya, L., Meissner, B., Riedl, M. C., Muik, M., Schwarzer, C., Ferraguti, F., Sarg, B., Lindner, H., Schweigreiter, R., Knaus, H. G., Romanin, C., & Bandtlow, C. E. (2013). Direct association of the reticulon protein RTN1A with the ryanodine receptor 2 in neurons. *Biochimica et Biophysica Acta*, *1833*(6), 1421. https://doi.org/10.1016/J.BBAMCR.2013.02.012

Kiss, A., Fischer, I., Kleele, T., Misgeld, T., & Propst, F. (2018). Neuronal growth cone size-dependent and -independent parameters of microtubule polymerization. *Frontiers in Cellular Neuroscience*, *12*, 195. https://doi.org/10.3389/FNCEL.2018.00195/FULL

Koppers, M., Özkan, N., Nguyen, H. H., Jurriens, D., McCaughey, J., Nguyen, D. T. M., Li, C. H., Stucchi, R., Altelaar, M., MacGillavry, H. D., Kapitein, L. C., Hoogenraad, C. C., & Farías, G. G. (2024). Axonal endoplasmic reticulum tubules control local translation via P180/RRBP1-mediated ribosome interactions. *Developmental Cell*, *0*(0). https://doi.org/10.1016/j.devcel.2024.05.005

Krijnse-Locker, J., Parton, R. G., Fuller, S. D., Griffiths, G., & Dotti, C. G. (1995). The organization of the endoplasmic reticulum and the intermediate compartment in cultured rat hippocampal neurons. *Molecular Biology of the Cell*, *6*(10), 1315–1332. https://doi.org/10.1091/mbc.6.10.1315

Kuo, Y. W., & Howard, J. (2021). Cutting, Amplifying, and Aligning Microtubules with Severing Enzymes. *Trends in Cell Biology*, *31*(1), 50. https://doi.org/10.1016/J.TCB.2020.10.004

Kuo, Y. W., Trottier, O., Mahamdeh, M., & Howard, J. (2019a). Spastin is a dual-function enzyme that severs microtubules and promotes their regrowth to increase the number and mass of microtubules. *Proceedings of the National Academy of Sciences of the United States of America*, *116*(12), 5533–5541. https://doi.org/10.1073/PNAS.1818824116/SUPPL_FILE/PNAS.1818824116.SM03.AVI

Kuo, Y. W., Trottier, O., Mahamdeh, M., & Howard, J. (2019b). Spastin is a dual-function enzyme that severs microtubules and promotes their regrowth to increase the number and mass of microtubules. *Proceedings of the National Academy of Sciences of the United States of America*, *116*(12), 5533–5541. https://doi.org/10.1073/PNAS.1818824116

Lee, M., Paik, S. K., Lee, M. J., Kim, Y. J., Kim, S., Nahm, M., Oh, S. J., Kim, H. M., Yim, J., Lee, C. J., Bae, Y. C., & Lee, S. (2009). Drosophila Atlastin regulates the stability of muscle microtubules and is required for synapse development. *Developmental Biology*, *330*(2), 250–262. https://doi.org/10.1016/J.YDBIO.2009.03.019

Lin, H.-M., Kuang, J.-X., Sun, P., Li, N., Lv, X., & Zhang, Y.-H. (2018). Reconstruction of Intratelencephalic Neurons in the Mouse Secondary Motor Cortex Reveals the Diverse Projection Patterns of Single Neurons. *Frontiers in Neuroanatomy*, *12*. https://doi.org/10.3389/fnana.2018.00086

Lin, Y. F., Xie, Z., Zhou, J., Chen, H. H., Shao, W. W., & Lin, H. D. (2019). Effect of exogenous spastin combined with polyethylene glycol on sciatic nerve injury. *Neural Regeneration Research*, *14*(7), 1271–1279. https://doi.org/10.4103/1673-5374.251336

Liu, B., Liu, S., & Sun, D. (2023). Low-Dose Taxol Promotes Neuronal Axons Extension and Functional Recovery after Spinal Cord Injury. *Mediators of Inflammation*, *2023*, 5604103. https://doi.org/10.1155/2023/5604103

Liu, Q., Yang, H., Luo, J., Peng, C., Wang, K., Zhang, G., Lin, H., & Ji, Z. (2024). 14-3-3 protein augments the protein stability of phosphorylated spastin and promotes the recovery of spinal cord injury through its agonist intervention. *ELife*, *12*. https://doi.org/10.7554/eLife.90184

Liz, M. A., Mar, F. M., Santos, T. E., Pimentel, H. I., Marques, A. M., Morgado, M. M., Vieira, S., Sousa, V. F., Pemble, H., Wittmann, T., Sutherland, C., Woodgett, J. R., & Sousa, M. M. (2014). Neuronal deletion of GSK3β increases microtubule speed in the growth cone

and enhances axon regeneration via CRMP-2 and independently of MAP1B and CLASP2. *BMC Biology*, *12*(1), 1–19. https://doi.org/10.1186/1741-7007-12-47/FIGURES/8

Lopez-Verrilli, M. A., Picou, F., & Court, F. A. (2013). Schwann cell-derived exosomes enhance axonal regeneration in the peripheral nervous system. *GLIA*. https://doi.org/10.1002/glia.22558

Luarte, A., Cornejo, V. H., Bertin, F., Gallardo, J., & Couve, A. (2018a). The axonal endoplasmic reticulum: One organelle—many functions in development, maintenance, and plasticity. In *Developmental Neurobiology*. https://doi.org/10.1002/dneu.22560

Luarte, A., Cornejo, V. H., Bertin, F., Gallardo, J., & Couve, A. (2018b). The axonal endoplasmic reticulum: One organelle—many functions in development, maintenance, and plasticity. In *Developmental Neurobiology*. https://doi.org/10.1002/dneu.22560

Maciel, R., Bis, D. M., Rebelo, A. P., Saghira, C., Züchner, S., & Saporta, M. A. (2018). The human motor neuron axonal transcriptome is enriched for transcripts related to mitochondrial function and microtubule-based axonal transport. *Experimental Neurology*, *307*, 155. https://doi.org/10.1016/J.EXPNEUROL.2018.06.008

Mannan, A. U., Boehm, J., Sauter, S. M., Rauber, A., Byrne, P. C., Neesen, J., & Engel, W. (2006a). Spastin, the most commonly mutated protein in hereditary spastic paraplegia interacts with Reticulon 1 an endoplasmic reticulum protein. *Neurogenetics*. https://doi.org/10.1007/s10048-006-0034-4

Mannan, A. U., Boehm, J., Sauter, S. M., Rauber, A., Byrne, P. C., Neesen, J., & Engel, W. (2006b). Spastin, the most commonly mutated protein in hereditary spastic paraplegia interacts with Reticulon 1 an endoplasmic reticulum protein. *Neurogenetics*, *7*(2), 93–103. https://doi.org/10.1007/s10048-006-0034-4

Mannan, A. U., Boehm, J., Sauter, S. M., Rauber, A., Byrne, P. C., Neesen, J., & Engel, W. (2006c). Spastin, the most commonly mutated protein in hereditary spastic paraplegia interacts with Reticulon 1 an endoplasmic reticulum protein. *Neurogenetics*, *7*(2), 93–103. https://doi.org/10.1007/S10048-006-0034-4

Matamoros, A. J., Tom, V. J., Wu, D., Rao, Y., Sharp, D. J., & Baas, P. W. (2019). Knockdown of Fidgetin Improves Regeneration of Injured Axons by a Microtubule-Based Mechanism. *Journal of Neuroscience*, *39*(11), 2011–2024. https://doi.org/10.1523/JNEUROSCI.1888-18.2018

McCurdy, E. P., Chung, K. M., Benitez-Agosto, C. R., & Hengst, U. (2019). Promotion of Axon Growth by the Secreted End of a Transcription Factor. *Cell Reports*, *29*(2), 363. https://doi.org/10.1016/J.CELREP.2019.08.101

Nijssen, J., Aguila, J., Hoogstraaten, R., Kee, N., & Hedlund, E. (2018). Axon-Seq Decodes the Motor Axon Transcriptome and Its Modulation in Response to ALS. *Stem Cell Reports*, *11*(6), 1565. https://doi.org/10.1016/J.STEMCR.2018.11.005

Nozumi, M., Togano, T., Takahashi-Niki, K., Lu, J., Honda, A., Taoka, M., Shinkawa, T., Koga, H., Takeuchi, K., Isobe, T., & Igarashi, M. (2009). Identification of functional marker proteins in the mammalian growth cone. *Proceedings of the National Academy of Sciences of the United States of America*, *106*(40), 17211–17216. https://doi.org/10.1073/pnas.0904092106

Pacheco, A., Merianda, T. T., Twiss, J. L., & Gallo, G. (2020). Mechanism and role of the intra-axonal Calreticulin translation in response to axonal injury. *Experimental Neurology*. https://doi.org/10.1016/j.expneurol.2019.113072

Pavez, M., Thompson, A. C., Arnott, H. J., Mitchell, C. B., D'Atri, I., Don, E. K., Chilton, J. K., Scott, E. K., Lin, J. Y., Young, K. M., Gasperini, R. J., & Foa, L. (2019). STIM1 is required for remodeling of the endoplasmic reticulum and microtubule cytoskeleton in steering growth cones. *Journal of Neuroscience*. https://doi.org/10.1523/JNEUROSCI.2496-18.2019

Petrova, V., Pearson, C. S., Ching, J., Tribble, J. R., Solano, A. G., Yang, Y., Love, F. M., Watt, R. J., Osborne, A., Reid, E., Williams, P. A., Martin, K. R., Geller, H. M., Eva, R., & Fawcett, J. W. (2020). Protrudin functions from the endoplasmic reticulum to support axon regeneration in the adult CNS. *Nature Communications 2020 11:1*, *11*(1), 1–15. https://doi.org/10.1038/s41467-020-19436-y

Rao, K., Stone, M. C., Weiner, A. T., Gheres, K. W., Zhou, C., Deitcher, D. L., Levitan, E. S., & Rolls, M. M. (2016a). Spastin, atlastin, and ER relocalization are involved in axon but not dendrite regeneration. *Molecular Biology of the Cell*. https://doi.org/10.1091/mbc.E16-05-0287

Rao, K., Stone, M. C., Weiner, A. T., Gheres, K. W., Zhou, C., Deitcher, D. L., Levitan, E. S., & Rolls, M. M. (2016b). Spastin, atlastin, and ER relocalization are involved in axon but not dendrite regeneration. *Molecular Biology of the Cell*. https://doi.org/10.1091/mbc.E16-05-0287

Rao, K., Stone, M. C., Weiner, A. T., Gheres, K. W., Zhou, C., Deitcher, D. L., Levitan, E. S., & Rolls, M. M. (2016c). Spastin, atlastin, and ER relocalization are involved in axon but not dendrite regeneration. *Molecular Biology of the Cell*. https://doi.org/10.1091/mbc.E16-05-0287

Rao, K., Stone, M. C., Weiner, A. T., Gheres, K. W., Zhou, C., Deitcher, D. L., Levitan, E. S., & Rolls, M. M. (2016d). Spastin, atlastin, and ER relocalization are involved in axon but not dendrite regeneration. *Molecular Biology of the Cell*. https://doi.org/10.1091/mbc.E16-05-0287

Reali, V., Mehdawy, B., Nardacci, R., Filomeni, G., Risuglia, A., Rossin, F., Antonioli, M., Marsella, C., Fimia, G. M., Piacentini, M., & Di Sano, F. (2015). Reticulon protein-1C is a key component of MAMs. *Biochimica et Biophysica Acta*, *1853*(3), 733–745. https://doi.org/10.1016/J.BBAMCR.2014.12.031

Roebroek, A. J. M., Van De Velde, H. J. K., Van Bokhoven, A., Broers, J. L. V, Ramaekers, F. C. S., & Van De Ven, W. J. M. (1993a). Cloning and expression of alternative transcripts of a novel neuroendocrine-specific gene and identification of its 135-kDa translational product. *Journal of Biological Chemistry*, *268*(18), 13439–13447.

Roebroek, A. J. M., Van De Velde, H. J. K., Van Bokhoven, A., Broers, J. L. V, Ramaekers, F. C. S., & Van De Ven, W. J. M. (1993b). Cloning and expression of alternative transcripts of a novel neuroendocrine-specific gene and identification of its 135-kDa translational product. *Journal of Biological Chemistry*, *268*(18), 13439–13447.

Roll-Mecak, A., & Vale, R. D. (2008). Structural basis of microtubule severing by the hereditary spastic paraplegia protein spastin. *Nature*. https://doi.org/10.1038/nature06482

Rolls, M. M., Thyagarajan, P., & Feng, C. (2020). Microtubule dynamics in healthy and injured neurons. *Developmental Neurobiology*, *81*(3), 321. https://doi.org/10.1002/DNEU.22746

Rotem, N., Magen, I., Ionescu, A., Gershoni-Emek, N., Altman, T., Costa, C. J., Gradus, T., Pasmanik-Chor, M., Willis, D. E., Ben-Dov, I. Z., Hornstein, E., & Perlson, E. (2017). ALS Along the Axons - Expression of Coding and Noncoding RNA Differs in Axons of ALS models. *Scientific Reports*, *7*. https://doi.org/10.1038/SREP44500

Saal, L., Briese, M., Kneitz, S., Glinka, M., & Sendtner, M. (2014). Subcellular transcriptome alterations in a cell culture model of spinal muscular atrophy point to widespread defects in axonal growth and presynaptic differentiation. *RNA (New York, N.Y.)*, *20*(11), 1789–1802. https://doi.org/10.1261/RNA.047373.114

Sahu, R., Kaushik, S., Clement, C. C., Cannizzo, E. S., Scharf, B., Follenzi, A., Potolicchio, I., Nieves, E., Cuervo, A. M., & Santambrogio, L. (2011). Microautophagy of Cytosolic Proteins by Late Endosomes. *Developmental Cell*, *20*(1), 131–139. https://doi.org/10.1016/J.DEVCEL.2010.12.003

Sasaki, Y., Welshhans, K., Wen, Z., Yao, J., Xu, M., Goshima, Y., Zheng, J. Q., & Bassell, G. J. (2010). Phosphorylation of Zipcode Binding Protein 1 Is Required for Brain-Derived Neurotrophic Factor Signaling of Local -Actin Synthesis and Growth Cone Turning. *Journal of Neuroscience*, *30*(28), 9349–9358. https://doi.org/10.1523/JNEUROSCI.0499-10.2010

Sengottuvel, V., Leibinger, M., Pfreimer, M., Andreadaki, A., & Fischer, D. (2011). Taxol Facilitates Axon Regeneration in the Mature CNS. *Journal of Neuroscience*, *31*(7), 2688–2699. https://doi.org/10.1523/JNEUROSCI.4885-10.2011

Shigeoka, T., Jung, H., Jung, J., Turner-Bridger, B., Ohk, J., Lin, J. Q., Amieux, P. S., & Holt, C. E. (2016). Dynamic Axonal Translation in Developing and Mature Visual Circuits. *Cell*, *166*(1), 181–192. https://doi.org/10.1016/j.cell.2016.05.029

Shigeoka, T., Koppers, M., Wong, H. H. W., Lin, J. Q., Cagnetta, R., Dwivedy, A., de Freitas Nascimento, J., van Tartwijk, F. W., Ströhl, F., Cioni, J. M., Schaeffer, J., Carrington, M., Kaminski, C. F., Jung, H., Harris, W. A., & Holt, C. E. (2019). On-Site Ribosome Remodeling by Locally Synthesized Ribosomal Proteins in Axons. *Cell Reports*, *29*(11), 3605-3619.e10. https://doi.org/10.1016/j.celrep.2019.11.025

Sholl, D. A. (1953). Dendritic organization in the neurons of the visual and motor cortices of the cat. *Journal of Anatomy*, *87*(Pt 4), 387. https://pmc.ncbi.nlm.nih.gov/articles/PMC1244622/

Solowska, J. M., Rao, A. N., & Baas, P. W. (2017). Truncating mutations of SPAST associated with hereditary spastic paraplegia indicate greater accumulation and toxicity of the M1 isoform of spastin. *Molecular Biology of the Cell*, *28*(13), 1728. https://doi.org/10.1091/MBC.E17-01-0047

Song, W., Cho, Y., Watt, D., & Cavalli, V. (2015). Tubulin-tyrosine ligase (TTL)-mediated increase in tyrosinated α-tubulin in injured axons is required for retrograde injury signaling and axon regeneration. *Journal of Biological Chemistry*, *290*(23), 14765–14775. https://doi.org/10.1074/jbc.M114.622753

Stepanova, T., Slemmer, J., Hoogenraad, C. C., Lansbergen, G., Dortland, B., De Zeeuw, C. I., Grosveld, F., Van Cappellen, G., Akhmanova, A., & Galjart, N. (2003). Visualization of Microtubule Growth in Cultured Neurons via the Use of EB3-GFP (End-Binding Protein 3-Green Fluorescent Protein). *Journal of Neuroscience*, *23*(7), 2655–2664. https://doi.org/10.1523/JNEUROSCI.23-07-02655.2003

Stepanova, T., Smal, I., Van Haren, J., Akinci, U., Liu, Z., Miedema, M., Limpens, R., Van Ham, M., Van Der Reijden, M., Poot, R., Grosveld, F., Mommaas, M., Meijering, E., & Galjart, N. (2010). History-dependent catastrophes regulate axonal microtubule behavior. *Current Biology*. https://doi.org/10.1016/j.cub.2010.04.024

Stone, M. C., Rao, K., Gheres, K. W., Kim, S., Tao, J., La Rochelle, C., Folker, C. T., Sherwood, N. T., & Rolls, M. M. (2012a). Normal Spastin Gene Dosage Is Specifically Required for Axon Regeneration. *Cell Reports*, *2*(5), 1340–1350. https://doi.org/10.1016/j.celrep.2012.09.032

Stone, M. C., Rao, K., Gheres, K. W., Kim, S., Tao, J., La Rochelle, C., Folker, C. T., Sherwood, N. T., & Rolls, M. M. (2012b). Normal Spastin Gene Dosage Is Specifically Required for Axon Regeneration. *Cell Reports*, *2*(5), 1340–1350. https://doi.org/10.1016/j.celrep.2012.09.032

Stone, M. C., Rao, K., Gheres, K. W., Kim, S., Tao, J., La Rochelle, C., Folker, C. T., Sherwood, N. T., & Rolls, M. M. (2012c). Normal Spastin Gene Dosage Is Specifically Required for Axon Regeneration. *Cell Reports*, *2*(5), 1340–1350. https://doi.org/10.1016/j.celrep.2012.09.032

Stone, M. C., Rao, K., Gheres, K. W., Kim, S., Tao, J., La Rochelle, C., Folker, C. T., Sherwood, N. T., & Rolls, M. M. (2012d). Normal spastin gene dosage is specifically required for axon regeneration. *Cell Reports*, *2*(5), 1340–1350. https://doi.org/10.1016/J.CELREP.2012.09.032

Taylor, A. M., Berchtold, N. C., Perreau, V. M., Tu, C. H., Li Jeon, N., & Cotman, C. W. (2009a). Axonal mRNA in Uninjured and Regenerating Cortical Mammalian Axons. *Journal of Neuroscience*, *29*(15), 4697–4707. https://doi.org/10.1523/JNEUROSCI.6130-08.2009

Taylor, A. M., Berchtold, N. C., Perreau, V. M., Tu, C. H., Li Jeon, N., & Cotman, C. W. (2009b). Axonal mRNA in Uninjured and Regenerating Cortical Mammalian Axons. *The Journal of Neuroscience*, *29*(15), 4697. https://doi.org/10.1523/JNEUROSCI.6130-08.2009

Taylor, A. M., Berchtold, N. C., Perreau, V. M., Tu, C. H., Li Jeon, N., & Cotman, C. W. (2009c). Axonal mRNA in Uninjured and Regenerating Cortical Mammalian Axons. *The Journal of Neuroscience*, *29*(15), 4697. https://doi.org/10.1523/JNEUROSCI.6130-08.2009

Taylor, A. M., Blurton-Jones, M., Rhee, S. W., Cribbs, D. H., Cotman, C. W., & Jeon, N. L. (2005). A microfluidic culture platform for CNS axonal injury, regeneration and transport. *Nature Methods*. https://doi.org/10.1038/nmeth777

Teixeira Lopes, A. (2018). *Spastin regulates microtubule dynamics and is required for normal motor and cognitive functions*.

Van De Velde, H. J. K., Roebroek, A. J. M., Senden, N. H. M., Ramaekers, F. C. S., & Van De Ven, W. J. M. (1994a). NSP-encoded reticulons, neuroendocrine proteins of a novel gene family associated with membranes of the endoplasmic reticulum. *Journal of Cell Science*, *107*(9), 2403–2416. https://doi.org/10.1242/JCS.107.9.2403

Van De Velde, H. J. K., Roebroek, A. J. M., Senden, N. H. M., Ramaekers, F. C. S., & Van De Ven, W. J. M. (1994b). NSP-encoded reticulons, neuroendocrine proteins of a novel gene family associated with membranes of the endoplasmic reticulum. *Journal of Cell Science*, *107*(9), 2403–2416. https://doi.org/10.1242/JCS.107.9.2403

Van Zundert, G. C. P., Rodrigues, J. P. G. L. M., Trellet, M., Schmitz, C., Kastritis, P. L., Karaca, E., Melquiond, A. S. J., Van Dijk, M., De Vries, S. J., & Bonvin, A. M. J. J. (2016). The HADDOCK2.2 Web Server: User-Friendly Integrative Modeling of Biomolecular Complexes. *Journal of Molecular Biology*, *428*(4), 720–725. https://doi.org/10.1016/J.JMB.2015.09.014

Voeltz, G. K., Prinz, W. A., Shibata, Y., Rist, J. M., & Rapoport, T. A. (2006). A class of membrane proteins shaping the tubular endoplasmic reticulum. *Cell*, *124*(3), 573–586. https://doi.org/10.1016/j.cell.2005.11.047

von Kügelgen, N., & Chekulaeva, M. (2020). Conservation of a core neurite transcriptome across neuronal types and species. *Wiley Interdisciplinary Reviews: RNA*, *11*(4), e1590. https://doi.org/10.1002/WRNA.1590;CTYPE:STRING:JOURNAL

Willis, D., Ka, W. L., Zheng, J. Q., Chang, J. H., Smit, A., Kelly, T., Merianda, T. T., Sylvester, J., Van Minnen, J., & Twiss, J. L. (2005). Differential transport and local translation of cytoskeletal, injury-response, and neurodegeneration protein mRNAs in axons. *Journal of Neuroscience*. https://doi.org/10.1523/JNEUROSCI.4235-04.2005

Wu, Y., Whiteus, C., Xu, C. S., Hayworth, K. J., Weinberg, R. J., Hess, H. F., & De Camilli, P. (2017). Contacts between the endoplasmic reticulum and other membranes in neurons. *Proceedings of the National Academy of Sciences of the United States of America*. https://doi.org/10.1073/pnas.1701078114

Yap, Y. C., King, A. E., Guijt, R. M., Jiang, T., Blizzard, C., Breadmore, M. C., & Dickson, T. C. (2017). Mild and repetitive very mild axonal stretch injury triggers cystoskeletal mislocalization and growth cone collapse. *PLOS ONE*, *12*(5), e0176997. https://doi.org/10.1371/JOURNAL.PONE.0176997

Zhang, Y., Chopp, M., Liu, X. S., Kassis, H., Wang, X., Li, C., An, G., & Zhang, Z. G. (2015). MicroRNAs in the axon locally mediate the effects of chondroitin sulfate proteoglycans and cGMP on axonal growth. *Developmental Neurobiology*, *75*(12), 1402–1419. https://doi.org/10.1002/dneu.22292

Zhang, Y., Ueno, Y., Liu, X. S., Buller, B., Wang, X., Chopp, M., & Zhang, Z. G. (2013a). The MicroRNA-17-92 cluster enhances axonal outgrowth in embryonic cortical neurons. *The Journal of Neuroscience : The Official Journal of the Society for Neuroscience*, *33*(16), 6885–6894. https://doi.org/10.1523/JNEUROSCI.5180-12.2013

Zhang, Y., Ueno, Y., Liu, X. S., Buller, B., Wang, X., Chopp, M., & Zhang, Z. G. (2013b). The MicroRNA-17–92 Cluster Enhances Axonal Outgrowth in Embryonic Cortical Neurons. *Journal of Neuroscience*, *33*(16), 6885–6894. https://doi.org/10.1523/JNEUROSCI.5180-12.2013

Acknowledgments: This research was partially supported by HPC OCÉANO (FONDEQUIP Nº EQM170214) and the supercomputing infrastructure of the NLHPC (CCSS210001). Centro Nacional de Inteligencia Artificial CENIA, FB210017, BASAL, ANID.

Funding:
ANID projects Fondecyt Initiation 11220601 (A.L.); EMBO scientific exchange grant 9218; EMBO short-stay Fellowship 8263

Author contributions.

Examples: AL, JPR
Conceptualization: AL, AC, RHM.
Methodology: AL, TA, APL, CG, CC, FB, JG, WA, AW, ACH, DC, JT,RV.
Investigation: AL, WZ, RHM, UH, CGR, ACH, AF, JPR.
Visualization: AL, CGR, AC, JT.
Supervision: AL, AC, UH, WZ, CG, APL.
Writing—original draft: AL, AC.
Writing—review & editing: AL, AC, CG, RHM, UW, CGR.

Competing interests: Authors declare that they have no competing interests.

Data and materials availability: All data needed to evaluate the conclusions in the paper will be available upon request.

1295 **Tables and Figures**
1296

Study	Neuron cell type	Model to obtain axonal fraction
(Saal et al., 2014)	Mice motor neurons	Spinal cord motor neurons cultured in microfluidic chambers (7 DIV).
(Rotem et al., 2017)	Mice motor neurons	Spinal cord motor neurons cultured in porous membrane inserts (10 DIV).
(Maciel et al., 2018)	iPSC-derived human motor neurons	Motor neurons were cultured on porous membrane inserts (10 DIV)
(Bigler et al., 2017)	Glutamatergic neurons differentiated from human embryonic stem cells (hESCs)	hESCs differentiated for 59 DIV in microfluidic chambers.
(Nijssen et al., 2018)	Human and mice motor neurons.	Spinal cord and human stem cell derived motor neurons were cultured in microfluidic chambers (7 and 14 DIV, respectively).
(Farias et al., 2020)	Rat mature myelinated motor neurons	Axoplasm microdissection of motor axons (*Ex vivo).*
(Gumy et al., 2011)	Rat embryonic/adult sensory neurons from dorsal root ganglion (DRG)	Primary neurons were cultured in microfluidic chambers (4 DIV).
(Taylor et al., 2009c)	Uninjured and regenerating rat cortical neurons	Primary neurons cultured in microfluidic chambers (10 DIV).

1297 **Table I.** Analyzed publications examining the transcriptome of an axon-enriched neuronal
1298 fraction. Days *in vitro* (DIV).
1299

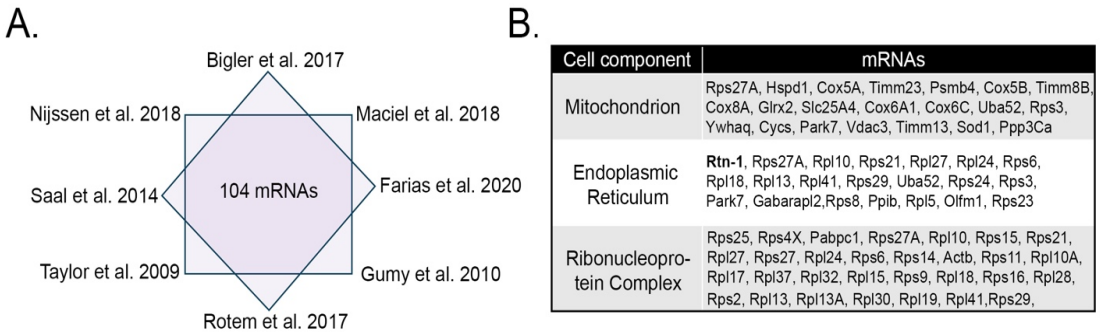

Cell component	mRNAs
Mitochondrion	Rps27A, Hspd1, Cox5A, Timm23, Psmb4, Cox5B, Timm8B, Cox8A, Glrx2, Slc25A4, Cox6A1, Cox6C, Uba52, Rps3, Ywhaq, Cycs, Park7, Vdac3, Timm13, Sod1, Ppp3Ca
Endoplasmic Reticulum	**Rtn-1**, Rps27A, Rpl10, Rps21, Rpl27, Rpl24, Rps6, Rpl18, Rpl13, Rpl41, Rps29, Uba52, Rps24, Rps3, Park7, Gabarapl2,Rps8, Ppib, Rpl5, Olfm1, Rps23
Ribonucleoprotein Complex	Rps25, Rps4X, Pabpc1, Rps27A, Rpl10, Rps15, Rps21, Rpl27, Rps27, Rpl24, Rps6, Rps14, Actb, Rps11, Rpl10A, Rpl17, Rpl37, Rpl32, Rpl15, Rps9, Rpl18, Rps16, Rpl28, Rps2, Rpl13, Rpl13A, Rpl30, Rpl19, Rpl41,Rps29,

1300
1301 **Figure 1. Analysis of diverse axonal transcriptomes reveals that *Rtn-1* mRNA is consistently**
1302 **identified**. **A.** Scheme illustrates studies of axonal transcriptomes and 104 shared mRNAs
1303 identified through a Benjamini–Hochberg (Ben) analysis. **B.** Table lists the category "Cellular
1304 Component" (Gene Ontology, GO) to classify the proteins coded by the 104 common mRNAs.
1305 The endoplasmic reticulum (ER) category only harbors *Rtn-1* (bold) as the only common mRNA
1306 coding for an ER structural protein.
1307
1308

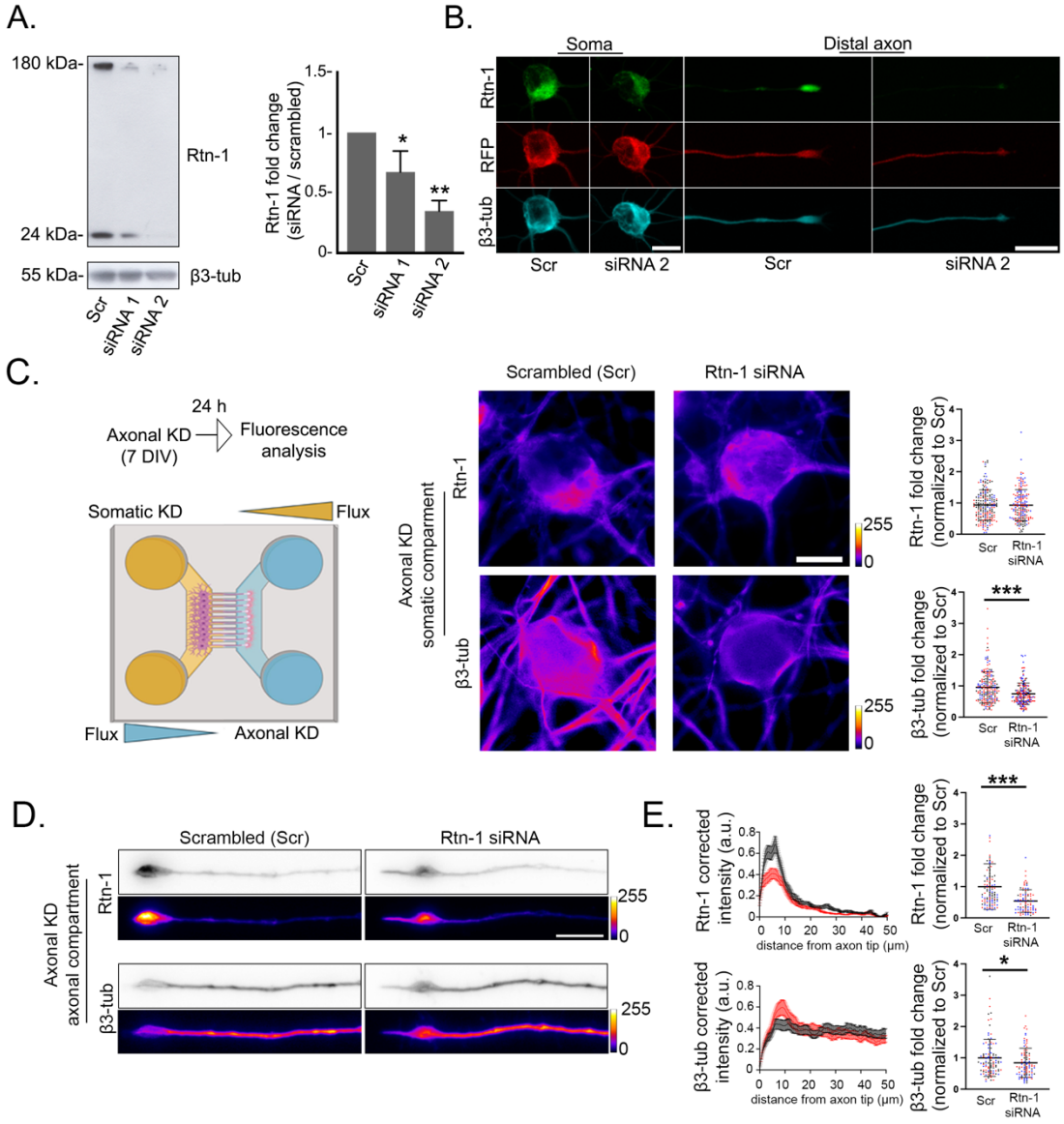

Figure 2. Axonal synthesis of Rtn-1 can be locally regulated in cortical neurons. A. *Left:* Western blot bands of Rtn-1 and β3-tubulin confirms the knockdown (KD) efficacy of siRNAs specifically designed against *Rtn-1* mRNA (Rtn-1 siRNA). 7 DIV Cortical neurons were transfected with Rtn-1 siRNAs and a control sequence (scrambled, Scr) for forty-eight hours. 20 µg of protein were loaded per lane, and β3-tubulin was used as loading control. *Right:* Graphs quantify the fold change of the lower Rtn-1 band after treatments with siRNAs 1-2 compared to Scr. Data are displayed as mean ± standard error of N = 6 biological replicates. Wilcoxon test compared to a theoretical mean of 1; $*p < 0.05$; $**p < 0.01$. **B.** Immunofluorescence images of the soma and distal axon of neurons stained against β3-tubulin and co-transfected with a plasmid encoding RFP and siRNA 2 or Scr under the same conditions indicated in A. Representative images from N= 4 independent experiments**.** Bar soma and axons=20 µm **C.** *Left:* schematic representation of the axonal KD strategy based on controlling volume differences between the compartment of microfluidic chambers. Under these conditions, 7 DIV cortical neurons were

selectively submitted to axonal treatments for twenty-four hours. *Right:* representative images and quantitative analysis of Rtn-1 and β3-tubulin intensity fold change in the cell bodies after axonal treatments. Bar =10 µm. Data are displayed as mean ± standard deviation (SD) of 229-300 neurons from N = 3 biological replicates. Linear mixed-effects model with experimental date included as a random effect; ∗∗∗$p < 0.001$. **D.** Immunofluorescence showing the intensity changes of Rtn-1 and β3-tubulin along the last 50 µm of axons locally treated with Rtn-1 siRNA or Scr. Bar =10 µm **E.** *Left:* corrected fluorescence intensity profiles of Rtn-1 and β3-tubulin from the last 50 µm of distal axons locally treated with Rtn-1 siRNA (red line) or Scr (black line). Intensity profiles depict the mean ± standard error from all the analyzed axons. *Right:* Bar graphs display the mean ± standard deviation of the fluorescence intensity fold change of 87-102 axons from N = 3 biological replicates. Linear mixed-effects model with experimental date included as a random effect; ∗$p < 0.05$; ∗∗∗$p < 0.001$.

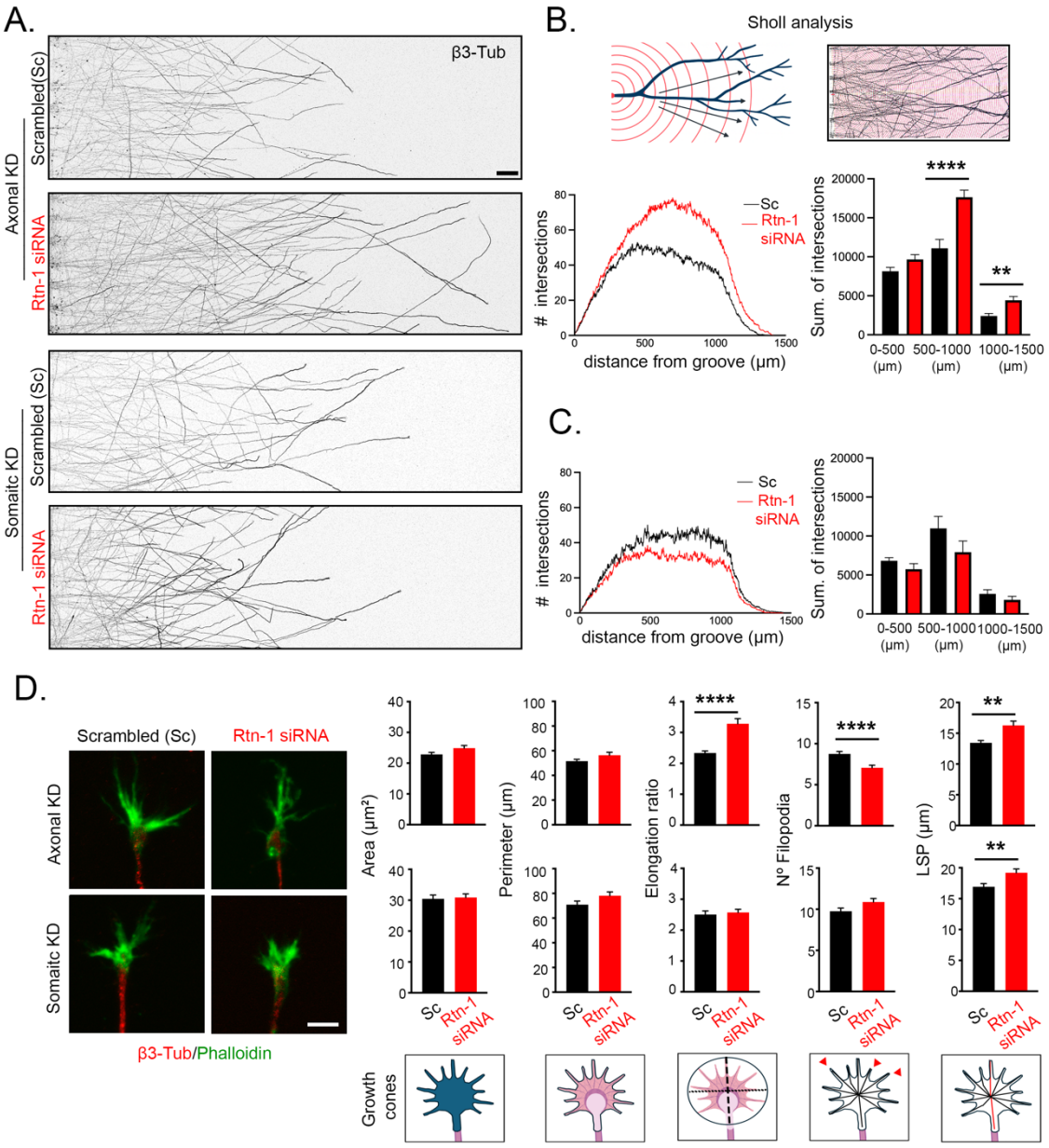

Figure 3. Axonal Rtn-1 knockdown (KD) promotes outgrowth and modify growth cone (GC) cytoskeleton after injury. A. Immunofluorescence against β3-tubulin in axons growing in microfluidic chambers twenty-four hours after injury (vacuum aspiration axotomy) comparing axonal and somatic Rtn-1 KD performed with a specific siRNA (Rtn-1-siRNA) or control sequence (scrambled, Scr). Bar= 50 µm. **B.** *Top:* schematic of an adapted Sholl analysis. Binarized axons were intersected with concentric semi-circles of increasing radius centered at the microgroove exit of the microfluidic chambers. *Bottom:* mean plots of the Sholl analyses performed after axonal Rtn-1 KD (red) compared to Scr (black). Bar graphs show the summatory of the total intersections within the indicated distance bins. **C.** Same analysis as in panel B but performed for somatic Rtn-1 KD. Data are displayed as mean ± standard error of 23-24 axonal fields from N = 6 biological replicates for axonal Rtn-1 KD; and 18-20 axonal fields from N=3 biological replicates for somatic Rtn-1 KD. Two-tailed Mann–Whitney *U* test; **p < 0.01; ****p

< 0.0001.**C.** Images show axonal growth cones after axonal or somatic Rtn-1 KD compared to Scr labeled against β3-tubulin (red) and Phalloidin (green) for staining the actine outline. Bar= 5 µm. Graphs depict the corresponding differences in GC area, perimeter, elongation ratio (or aspect ratio), number of filopodia, and longest shortest path (LSP), which corresponds to maximal distance calculated from the skeletonized outline (shown with the red line of the schematic drawings below). Data are displayed as mean ± standard error of 145-153 axons for axonal KD; 227-148 axons for somatic KD from N = 3 biological replicates. Two-tailed Mann–Whitney *U* test; $**p < 0.01$; $****p < 0.0001$.

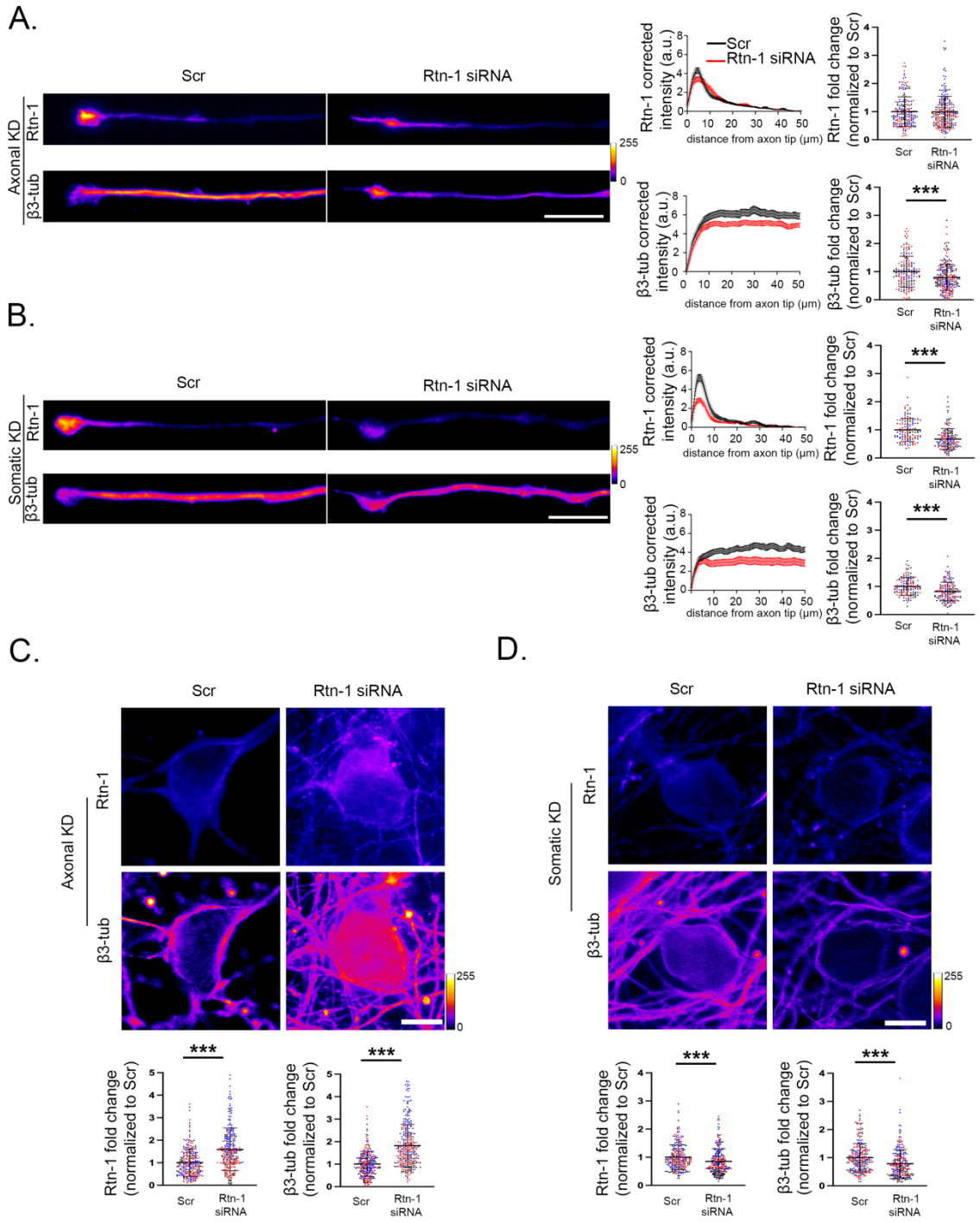

Figure 4. Axonal and somatic β3-tubulin levels are dependent on the local synthesis of Rtn-1 after injury. A. Left: immunofluorescence images and their corresponding corrected fluorescence intensity profiles along the last 50 μm of distal axons stained against Rtn-1 and β3-tubulin after axonal transfection with Rtn-1 siRNA (red; axonal Rtn-1 KD) or a control sequence (black; scrambled, Scr). Intensity profiles depict the mean ± standard deviation from all the analyzed axons. Bar = 10 μm. Right: bar graphs quantify the Rtn-1 and β3-tubulin fluorescence intensity fold change. Data are displayed as the mean ± standard deviation of 206–242 axons from

N = 3 biological replicates. Linear mixed-effects model with experimental date included as a random effect; ***$p < 0.001$.**B.** Same analysis as in panel A but performed for somatic Rtn-1 KD. Data are displayed as mean ± standard error of 133–161 axons from N = 3 biological replicates. Linear mixed-effects model with experimental date included as a random effect; ***$p < 0.001$. **C.** Images depict neuronal cell bodies stained for Rtn-1 and β3-tubulin after axonal Rtn-1 KD or Scr. Bar graphs depict Rtn-1 and β3-tubulin fluorescence intensity fold change displayed as mean ± standard error of 358–382 neurons from N = 3 biological replicates. Linear mixed-effects model with experimental date included as a random effect; ***$p < 0.001$. Bar = 10 µm. **D.** Same analysis as in panel C but performed for somatic Rtn-1 KD. Data are displayed as mean ± standard error of 252–237 neurons from N = 3 biological replicates. Linear mixed-effects model with experimental date included as a random effect;***<0.001. Bar = 10 µm.

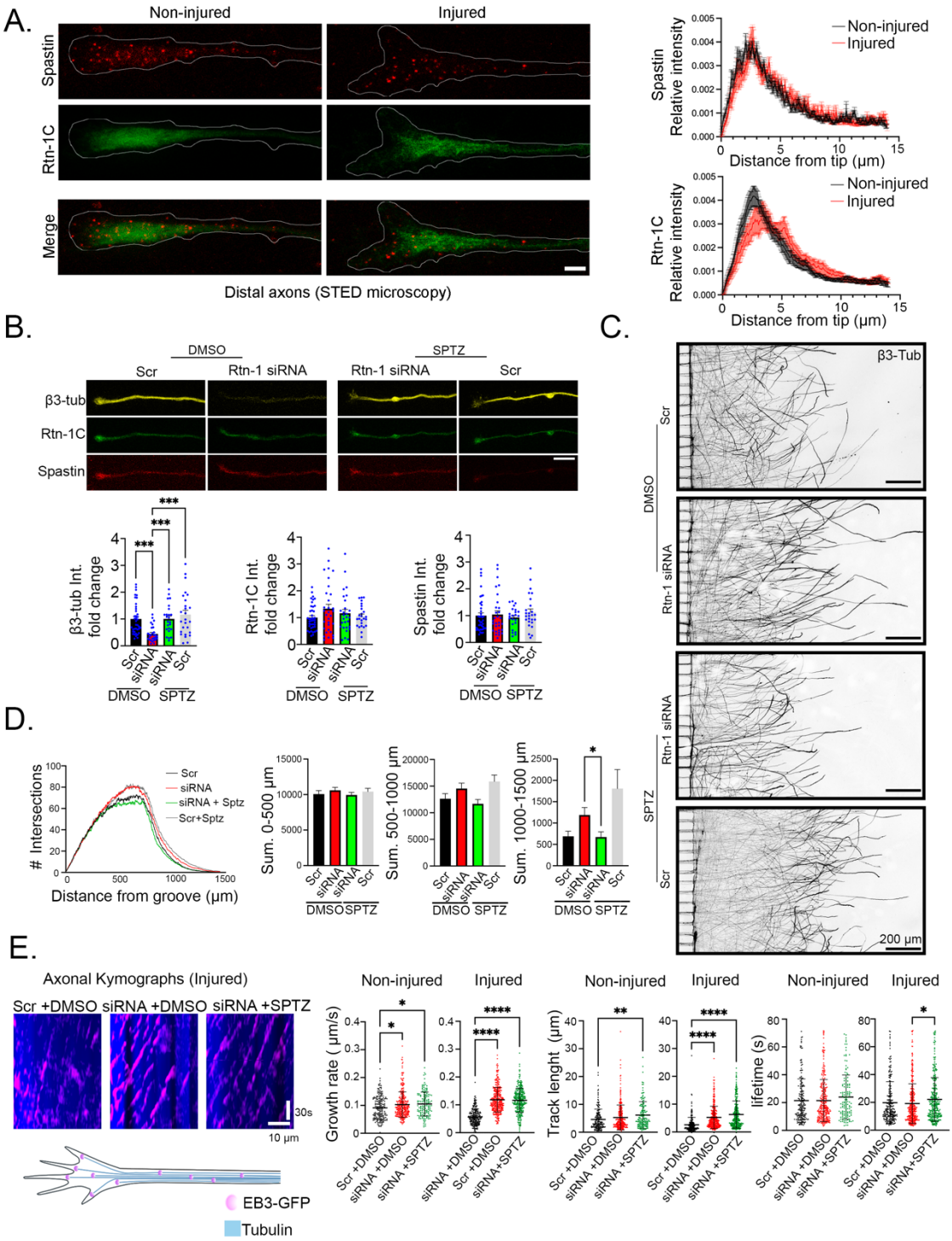

Figure 5. Axonal Rtn-1 KD after injury controls distal tubulin levels and outgrowth depending on Spastin's microtubule severing. **A.** *Left:* representative fluorescent super resolution STED images of distal non-injured and injured cortical axons (forty-four hours post-axotomy) in microfluidic chambers, which were stained against Rtn-1C (green), and Spastin (red), axon outlines are depicted (white lines). *Right:* Plots depict the relative fluorescence intensity profile (normalized against total distal intensity) of Rtn-1C and Spastin in non-injured (black) and injured (red) axons. Data are displayed as mean ± standard error of 9-13 axons from N=4

biological replicates. Bar= 5 µm **B.** *Top:* representative confocal images of distal axons stained against β3-tubulin (yellow), Rtn-1C (green), and Spastin (red) in microfluidic chambers forty-four hours post-axotomy under indicated treatments: controls (Scrambled, Scr +DMSO), Rtn-1 knockdown (Rtn-1 siRNA), and Spastin pharmacological inhibition with 50 nM Spastazoline (SPZT). Bar= 10 µm. *Bottom:* quantifications of fluorescence intensity fold change of indicated proteins in the last 50 µm compared to Scr. Data are displayed as mean ± standard error of 24-40 axons for condition from N=3 biological replicates. Kruskal–Wallis followed by Dunn's post hoc test; $***p < 0.001$.**C.** Illustrative axonal fields in microfluidic chambers forty-four hours post-axotomy stained against β3-tubulin under the treatments shown in B. Bar= 200 µm. **D.** Mean plots of the Sholl analyses performed with colored lines indicating the analyzed conditions. Bar graphs show the summatory of the total intersections within the indicated distance bins. Data are displayed as mean ± standard error of 22-24 axonal fields for condition from N=3 biological replicates. One-way ANOVA followed by Tukey's post hoc test; $*p < 0.05$. **E.** *Left:* axonal kymographs showing microtubule dynamics in neurons with indicated treatments forty-four hours after axotomy, dashes represent the traces of EB3-GFP (end-binding protein 3 fused to Emerald GFP). Scale bars represent 10 µm and 30 seconds, respectively. Analysis of microtubule dynamic parameters in non-injured and injured axons with indicated treatments: growth rate, track length, and lifetime of microtubule plus-end tracks. Data are displayed as mean ± standard error of 146-377 comets/dashes for condition from N=3 biological replicates. Kruskal–Wallis followed by Dunn's post hoc test; $*p < 0.05$; $**p < 0.01$; $****p < 0.001$.

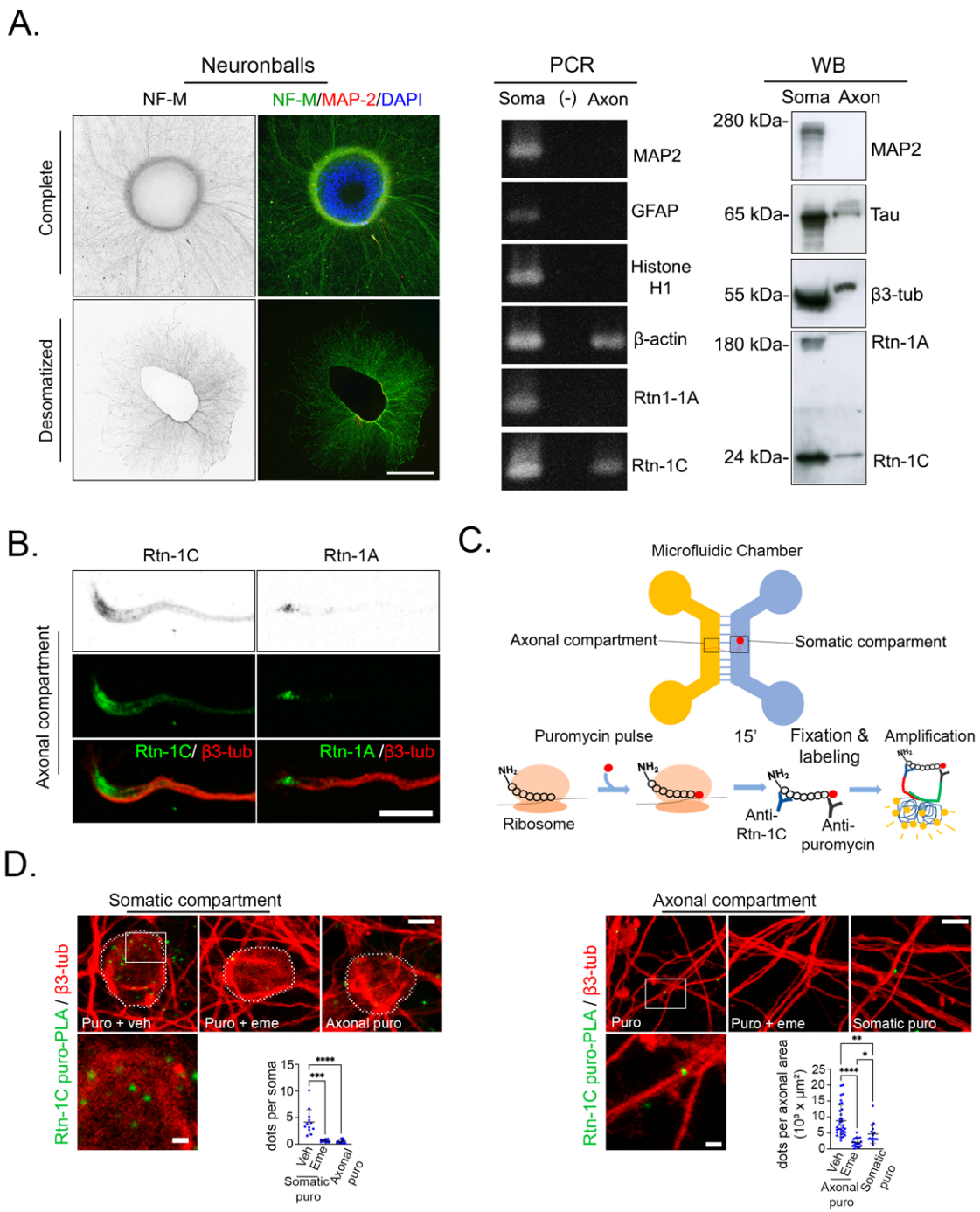

1406

1407 **Figure 6**. **Rtn-1C is locally synthesized in cortical axons**. **A.** *Left:* immunofluorescence of
1408 neuronballs stained against neurofilament medium chain (NF-M, grayscale and green) and
1409 Microtubule-associated protein 2 (MAP-2, red) with nuclei counterstaining (DAPI, blue). Top
1410 panel shows intact neuronballs, bottom panel shows neuronballs after mechanic removal of cell
1411 bodies. *Right:* RT- PCR analyses of axonal and somatic fractions of mRNAs coding for MAP2,
1412 glial fibrillary acidic protein (GFAP), histone H1, β-actin, Rtn-1C, and Rtn-1A. Western Blot
1413 analysis of the corresponding fractions using a pan-Rtn-1 antibody to reveal Rtn-1A and Rtn-1C
1414 isoforms, β3-tubulin (β3-tub), and Tau. Bar= 500 µm. Images and bands are representative of two
1415 independent experiments. **B.** Confocal images showing the expression of Rtn-1C and Rtn-1A

(green) and β3-tub (red) in the distal axonal compartment of microfluidic chambers. Bar= 10 µm. Images are representative of two independent experiments **C.** Schematic of the microfluidic chamber setup used to functionally isolate axonal and somatic compartments. Proximity ligation assay coupled to puromycylation (puro-PLA) is depicted below. Local puromycin (puro) incorporation into newly synthesized peptides allows amplification when puro is closed enough to the N-terminal. **D.** puro-PLA positive spots are shown in green at somatic and axonal compartments. β3-tubulin labeling depicts cell bodies and axons. Insets show higher magnification of PLA signals. Bar graphs quantify dot signals per cell bodies and per area in axons after local co-treatments of puro with the protein synthesis inhibitor emetine (Eme) or vehicle (Veh), or puro at the opposite compartment. Bar= 5 µm; inserts= 1 µm. Data are displayed as mean ± standard deviation of 11-12 somatic and 16-33 axonal fields from N=4 biological replicates. Kruskal–Wallis followed by Dunn´s post hoc test; *$p < 0.05$; **$p < 0.01$; ***$p < 0.001$;**** $p < 0.0001$.

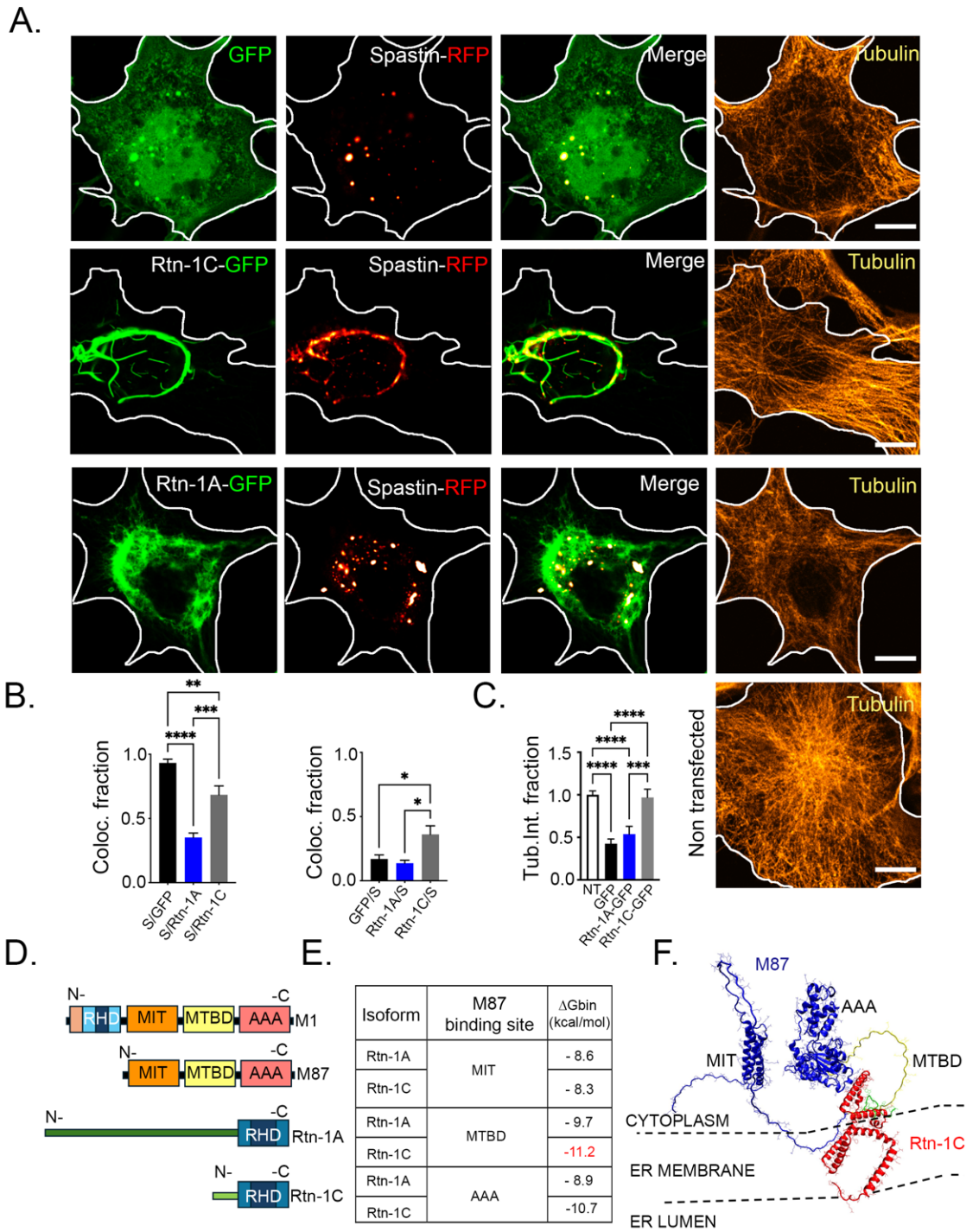

Isoform	M87 binding site	ΔGbin (kcal/mol)
Rtn-1A	MIT	- 8.6
Rtn-1C		- 8.3
Rtn-1A	MTBD	- 9.7
Rtn-1C		-11.2
Rtn-1A	AAA	- 8.9
Rtn-1C		-10.7

Figure 7. Rtn-1C co-distributes with Spastin and attenuates its microtubule-severing activity. A. Representative images of COS-7 cells expressing Spastin-RFP (fire red) together with GFP (green), Rtn-1A-GFP, or Rtn-1C-GFP, and immunostained against tubulin (yellow). While Spastin-RFP displays a punctate pattern when co-expressed with GFP or Rtn-1A-GFP, co-expression with Rtn-1C-GFP results in redistribution of Spastin signal along tubular ER-like structures. Bar=10 µm. **B.** Bar graphs show the indicated Mander's coefficients to quantify the colocalization between Spastin-RFP and GFP or Rtn-1 isoforms. Data are displayed as mean ± standard error from 9 cells per condition from N=2 biological replicates. One-way ANOVA with

1441 Tukey's post hoc test; *p < 0.05, **p < 0.01, ****p < 0.0001. **C.** Tubulin intensity fraction in
1442 cells expressing Spastin-RFP with GFP, Rtn-1A-GFP, or Rtn-1C-GFP compared to non-
1443 transfected cells. Rtn-1C co-expression counteracts the reduction in microtubule intensity induced
1444 by Spastin. Data are displayed as mean ± standard error from 145 non-transfected cells, 33
1445 Spastin-RFP/GFP cells, 35 Spastin-RFP/Rtn-1A-GFP cells, and 32 Spastin-RFP/Rtn-1C-GFP
1446 cells from N=2 biological replicates. One-way ANOVA with Tukey's post hoc test; *p < 0.05,
1447 **p < 0.01, ***p < 0.001, ****p < 0.0001. **D.** Domain organization of Spastin isoforms (M1 and
1448 M87) and Rtn-1 isoforms (Rtn-1A and Rtn-1C), including the Reticulon Homology Domain
1449 (RHD), Microtubule Interacting and Trafficking domain (MIT), Microtubule-Binding Domain
1450 (MTBD), and ATPases Associated with diverse cellular Activities (AAA) domain (severing
1451 domain). **E.** Predicted binding affinities (ΔG binding, kcal/mol) between Spastin M87 and Rtn-1
1452 isoforms at different domains, highlighting strong interactions with Rtn-1C. **F.** Structural model
1453 (VMD snapshots) of the predicted interaction between the MTBD (yellow) of Spastin M87 (blue)
1454 and the N-terminal region (green) of Rtn-1C (red).